

Topological Transformations of Biomembranes and Vesicles *via* Fission and Fusion

Reinhard Lipowsky

Max Planck Institute of Colloids and Interfaces,
Science Park Golm, 14424 Potsdam, Germany

Abstract

The cells of our body are compartmentalized by biomembranes and vesicles, which consist of molecular bilayers with a thickness of a few nanometers and which represent two-dimensional fluids. Because of their fluidity, the bilayer membranes can easily remodel their composition, shape, and topology. Here, we will focus on their topology and on transformations between different topologies *via* fission and fusion processes. In general, these topological transformations can be characterized by changes in the Euler characteristic and in the topological genus. Fission processes proceed via the closure and cleavage of membrane necks as recently demonstrated for giant unilamellar vesicles (GUVs) and for unilamellar nanovesicles assembled *in silico*. Neck cleavage is controlled by constriction forces that compress the neck and provide a general physical mechanism for membrane fission. Fusion processes proceed via the adhesion of two membranes and by the formation of a fusion pore, which has the same shape as a membrane neck. In fact, when two membranes fuse, they undergo the same sequence of shapes as during fission but in reversed order. However, the ‘local surgery’, necessary to form the fusion pore, involves alternative molecular pathways as reviewed here for tension-induced fusion. Multispherical vesicles, doped with membrane proteins that drive homotypic fusion, can be used to form high genus vesicles, which are accessible to experimental studies.

1 Introduction

Our body contains a huge number of biomembranes that enclose our cells and most intracellular organelles. These membranes are fluid and create a flexible architecture that partitions each cell into separate liquid compartments. This membrane architecture is rather dynamic and continuously remodeled. First, the flexibility of these membranes allows them to easily adapt both their local composition and their shape to different cues in their surroundings. Second, the membrane compartments can change their topology via fusion and fission processes. Thus, if we looked at the intracellular membrane compartments with nanoscopic resolution, we would see heavy traffic of vesicles between different organelles as displayed in Fig. 1. [1] This traffic involves both the production of new vesicles via budding and fission from a donor membrane as well as the uptake of such vesicles by acceptor membranes via adhesion and fusion.

In Fig. 1, the different membrane-bound organelles are displayed in a highly schematic manner. In particular, only the inner part of the endoplasmic reticulum (ER) is shown, which is known as the perinuclear region and is located close to the nuclear envelope. [2] Another particularly fascinating part of the ER is its peripheral region, which forms a network of membrane nanotubes that extend throughout the whole cell, as shown by the light microscopy image in Fig. 2a. The network consists of irregular polygons connected by three-way junctions with contact angles close to 120° [3, 4]

In spite of its complex architecture, the whole nanotubular network of the ER is formed by a single membrane which encloses a continuous nanofluidic network of water channels [2]. As a consequence, the ER membrane creates a bicontinuous structure that partitions the intracellular space into two separate, interpenetrating subcompartments, the lumen of the ER network and the surrounding cytosol. In fact, the ER membrane itself provides two additional quasi-2-dimensional subcompartments corresponding to the two leaflets of the lipid-protein bilayer, which can accommodate membrane-bound molecules and processes. All four subcompartments are fluid, which implies that widely separated regions of the cell can communicate with each other, both via the ER membrane and via the ER lumen.

From a topological point of view, the peripheral ER is rather fascinating because of its very large topological genus, corresponding to the huge number of irregular polygons formed by the ER membrane. The genus of the peripheral ER is quite stable over extended periods of time but is

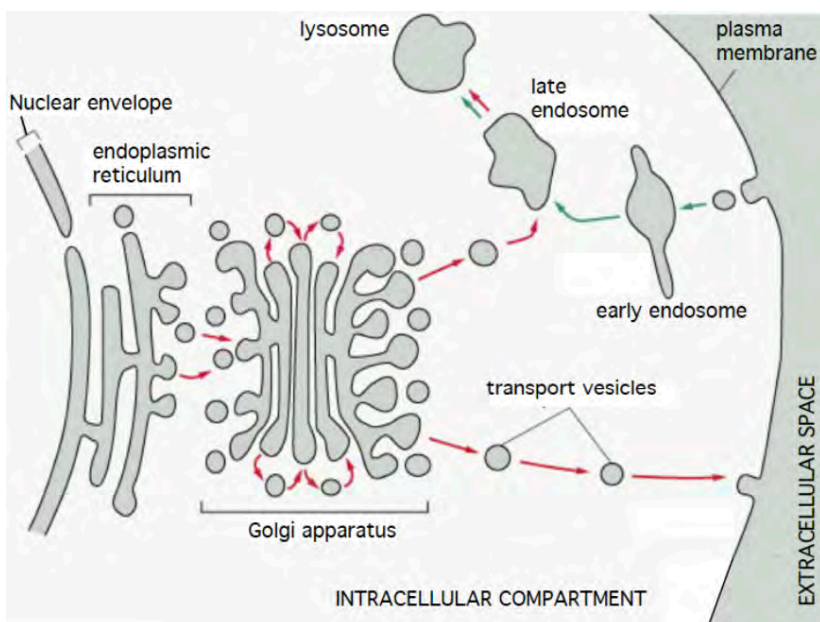


Figure 1: Schematic view of vesicular traffic within eukaryotic cells. Vesicles are formed by budding and fission from donor membranes, transported across the cell, and eventually integrated by adhesion and fusion into acceptor membranes. The red arrows indicate the outward secretory pathway, the green arrows the inward endocytic pathway. [1] With permission from W. W. Norton and Company.

occasionally remodeled by ring closure and tubule branching, see Fig. 2b. [4, 5] Ring closure deletes one polygon from the network, thereby decreasing the topological genus of the ER. Branching, on the other hand, creates one additional polygon, thereby increasing the topological genus. In vivo, these remodeling processes are controlled, at least to some extent, by interactions of the ER membranes with the cytoskeleton. On the other hand, in-vitro reconstitution of the peripheral ER has demonstrated that the nanotubular networks are also formed in the absence of any cytoskeletal elements.

In cell biology, a lot of effort has been devoted to identify the different membrane proteins that are involved in the topological transformations of cellular and intracellular membranes. These proteins perturb the membranes locally, thereby inducing their fission and fusion. In this review, we will use a coarse-grained description for the molecular details of this ‘local surgery’ and will focus on the membrane geometry of the remodeling processes and on the membrane elasticity which includes both their curvature elasticity and membrane tension. Furthermore, we will illustrate the geometric and membrane-elastic features for two types of synthetic membrane compartments, giant unilamellar vesicles (GUVs) as studied by light microscopy and nanovesicles as visualized by molecular dynamics simulations.

This review is organized as follows. We will first introduce, in Section 2, the Euler characteristic and the topological genus in order to obtain a general classification of the membrane topology and its topological transformations. Fission processes which reduce the genus and increase the Euler characteristic will be addressed in Section 3, where we emphasize the formation of membrane necks for out- and in-budded vesicles as well as the constriction forces compressing these necks. Section 4 describes three recent examples for fission processes that drive the division of GUVs, as observed by light microscopy, as well as the division of nanovesicles and their endocytosis of condensate droplets, as studied in molecular dynamics simulations. Fusion processes, which increase the genus and reduce the Euler characteristic, are considered in Section 5, focusing on the relatively simple mechanism of tension-induced fusion, which exhibits several fusion pathways. Section 6 is devoted to the fusion and fission of multispherical vesicles, which are useful in order to study higher genus vesicles, similar to the ER. The last Section 7 contains a summary and an outlook on related topics that provide challenges for future studies.

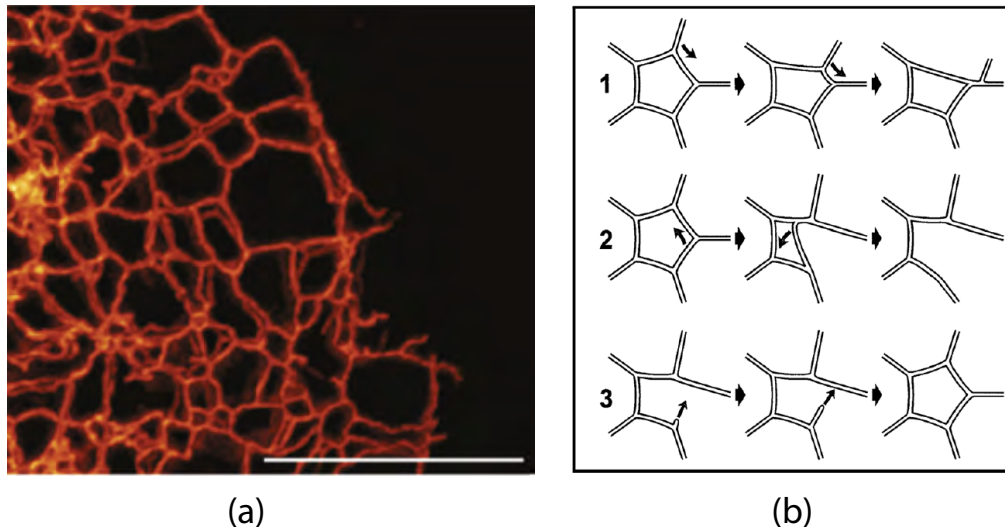


Figure 2: (a) Nanotubular network of the peripheral endoplasmic reticulum (ER) with a very high topological genus, which is equal to the number of irregular polygons formed by the membrane nanotubes. Scale bar: $10 \mu\text{m}$ [2] With permission from Jennifer Lipponcott-Schwartz; and (b) Dynamic processes of sliding, ring closure, and tubule branching as shown in row 1, 2, and 3. Ring closure removes one polygon from the network, thereby reducing the genus of the ER membrane, whereas tubule branching increases this genus by creating a new polygon. [5] With permission from International Review of Cytology, 2001.

2 Topology of closed membrane surfaces

The topology of a closed membrane surface can be characterized in a global manner, using the Euler characteristic χ or the topological genus \mathbf{g} , which are two integer numbers. To obtain the precise values of these numbers may be quite difficult, as one can envisage by looking at the reticular network in Fig. 2a. On the other hand, we can also focus on the ‘local surgery’ of the membrane by individual fission and fusion events, which change χ by ± 2 and \mathbf{g} by ± 1 . In the following subsections, we will first characterize topologically simple membrane surfaces with small χ - and \mathbf{g} -values in a global manner and subsequently look at the changes of χ and \mathbf{g} arising from the ‘local surgery’ of these surfaces.

2.1 Euler characteristic and topological genus

In general, the topology of any closed surface in three dimensions can be characterized by the integer Euler characteristic χ . This number can be obtained from any partitioning of the surface into a discrete set of surface segments. [6] One widely applied discretization method is triangulation but one may also use a mesh of smooth curves that are embedded in the surface. Any discretization involves the surface segments themselves, usually called ‘faces’, the edges between neighboring faces, and the vertices at which several edges come together. Counting the number of faces, F , the number of edges, E , and the number of vertices, V , the Euler characteristic χ is obtained via

$$\chi = F - E + V \quad (1)$$

The three numbers F , E , and V depend on the chosen partitioning of the surface, as one can easily see by using different polyhedra to discretize a sphere. In contrast, the Euler characteristic χ itself is independent of this partitioning and defines the topology of the surface. Thus, we obtain $\chi = 2$ for a tetrahedron, a cube or an icosahedron as well as for any other partitioning of a spherical surface.

Some examples for closed membrane surfaces with different χ -values are displayed in Fig. 3. The torus or doughnut surface has the Euler characteristic $\chi = 0$, the double-torus or button surface has $\chi = -2$ the sphere has $\chi = 2$, and the combined surface of two spheres has $\chi = 4$. Likewise the topology of N_{ve} spherical vesicles is characterized by $\chi = 2N_{\text{ve}}$ which extends the sequence of surface

topologies in Fig. 3 to the left. Furthermore, a membrane surface, which forms \mathbf{g} handles or loops, has $\chi = 2 - 2\mathbf{g}$, which extends the surface topologies in Fig. 3 to the right.¹

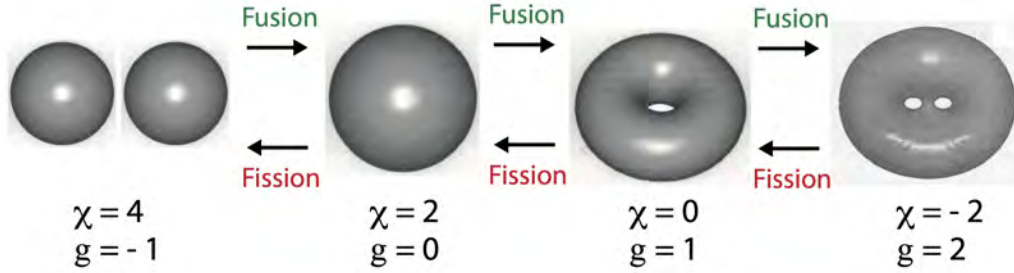


Figure 3: Closed membrane surfaces with different topologies, distinguished by their Euler characteristic χ and their topological genus \mathbf{g} : Two spherical vesicles are characterized by $\chi = 4$ and $\mathbf{g} = -1$; a single spherical vesicle by $\chi = 2$ and $\mathbf{g} = 0$; a torus (or doughnut shape) by $\chi = 0$ and $\mathbf{g} = 1$; and a double torus (or button shape) by $\chi = -2$ and $\mathbf{g} = 2$. Membrane fusion decreases the Euler characteristic χ and increases the topological genus \mathbf{g} whereas membrane fission increases χ and decreases \mathbf{g} . Additional fission events lead to more spherical vesicles with a large and positive χ . Additional fusion events lead to a membrane surface with a large number of handles, corresponding to a large and positive \mathbf{g} , see the reticular network in Fig. 2a. The formation of membrane surfaces with $\mathbf{g} \geq 1$ involves self-adhesion of the membrane.

The number \mathbf{g} of handles or loops provides another, equivalent characterization of a closed surface, the so-called topological genus \mathbf{g} , which satisfies

$$\mathbf{g} = 1 - \frac{1}{2} \chi \quad \text{and} \quad \Delta \mathbf{g} = -\frac{1}{2} \Delta \chi \quad (2)$$

where $\Delta \mathbf{g} \equiv \mathbf{g}_2 - \mathbf{g}_1$ and $\Delta \chi \equiv \chi_2 - \chi_1$ is the difference between the genera of two surfaces 1 and 2 and between their Euler characteristics. For a sphere and a torus, the topological genus is equal to $\mathbf{g} = 0$ and $\mathbf{g} = 1$, respectively. The topological genus \mathbf{g} can be deduced directly from the global surface geometry by counting the number of handles or loops formed by the surface, without any partitioning or discretization of this surface. Thus, when we look at the nanotubular network of the peripheral endoplasmic reticulum in Fig. 2a, we can immediately conclude that this network has a very large and positive genus \mathbf{g} and, thus, a very large and negative Euler characteristic χ .

2.2 Local topology changes by fission and fusion

By definition, a topological transformation of a vesicle or another closed membrane compartment implies that this compartment changes its topology and, thus, its Euler characteristic and topological genus. In the living cell, the membrane-bound organelles continuously undergo such topological transformations by membrane fission and membrane fusion, as illustrated in Fig. 1. Likewise, the simple topologies in Fig. 3 can be transformed into each other by individual fusion and fission processes. These individual events proceed via some ‘local surgery’ which can be characterized without knowing the global shape and topology of the membrane compartment.

A single, local *fission* event as depicted in Fig. 4a,b leads to an increase of the Euler characteristic by $\Delta \chi = +2$ and to a decrease of the topological genus by $\Delta \mathbf{g} = -\frac{1}{2} \Delta \chi = -1$. On the other hand, a single, local *fusion* event leads to a decrease of the Euler characteristic by $\Delta \chi = -2$ and to an increase of the genus by $\Delta \mathbf{g} = +1$, see Fig. 4c,d. These positive and negative values of $\Delta \chi$ and $\Delta \mathbf{g}$ for single fission and fusion events are completely general and apply to any shape and topology of the membrane compartment as long as this compartment forms a closed surface without bilayer pores or bilayer edges, both before and after such an event. Therefore, computing the Euler characteristic before and after a topological transformation provides a simple and general method to distinguish fission and fusion processes which may not be obvious otherwise.

¹Handles or loops are sometimes called ‘pores’ but, for biomembranes, a ‘pore’ is a water channel across the bilayer membrane.

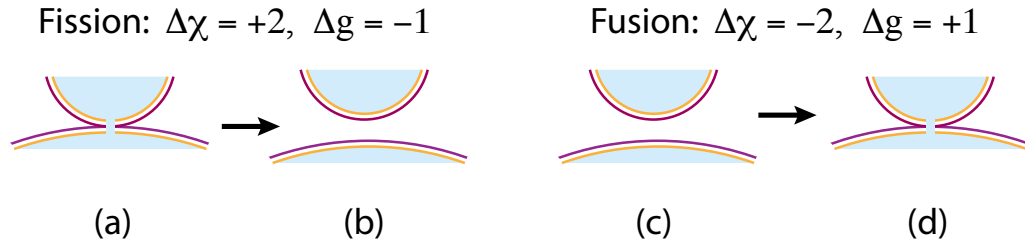


Figure 4: ‘Local surgery’ of membrane topology by single fission and fusion events: (a) A single fission event proceeds via the formation and cleavage of a membrane neck; (b) After neck cleavage, the Euler characteristic χ and the topological genus g of the membrane compartment have been changed by $\Delta\chi = +2$ and $\Delta g = -1$; (c) A single fusion event proceeds via the adhesion of two membrane segments and the formation of a fusion pore; and (d) After the fusion pore has been formed, the Euler characteristic and the genus of the membrane compartment have been changed by $\Delta\chi = -2$ and $\Delta g = +1$. These changes of χ and g apply irrespective of the overall shape and global topology of the compartment. Biomembranes are molecular bilayers with two leaflets, which typically have a certain transbilayer asymmetry as indicated by the two colors purple and orange for the outer and inner leaflets. The light blue aqueous solution in contact with the inner leaflet (orange) represents the lumen of the compartment.

3 Fission via budding and neck cleavage

A single fission event as displayed in Fig. 4a,b proceeds in several steps. First, the mother or donor membrane forms a bud which is still connected to the donor membrane by a narrow or closed membrane neck. Second, the bilayer membrane is cleaved across this neck, thereby forming two bilayer edges in contact with the aqueous solutions. Third, these bilayer edges are resealed which leads to a donor membrane with reduced membrane area and to a newly formed daughter vesicle. In order to obtain additional insight into the formation and stability of the membrane neck, we will first consider the simplest case as provided by the fission of a vesicle with genus $g = 0$ which has the topology of a sphere. For genus-0 vesicles, the fission process has been studied in some detail, both by analytical theory, experiment, and simulations. [7, 8, 9, 10] The two substeps, formation and cleavage of a membrane neck will now be described in more detail.

3.1 Two budding geometries for genus-0 vesicles

For genus-0 vesicles, the formation of a membrane bud can proceed in two different ways as shown in Fig. 5. First, the vesicle membrane may form an out-bud as depicted in Fig. 5a. The out-bud represents a membrane deformation towards the exterior space which is still connected to the mother vesicle by a closed membrane neck. Second, the vesicle membrane can form an in-bud as in Fig. 5c. The in-bud points towards the interior vesicle compartment, again connected to the mother vesicle by a closed membrane neck.²

The formation of an out-bud and the subsequent cleavage of the membrane neck leads to two daughter vesicles that are ‘mutually disjoint’ in the sense that they enclose two disjoint spatial regions. Furthermore, the two daughter vesicles arising from an out-bud have the same bilayer asymmetry as the mother vesicle. In contrast, the formation of an in-bud and the subsequent neck fission leads to two daughter vesicles that are ‘nested’ in the sense that the spatial region enclosed by the larger daughter vesicle includes the smaller one. In addition, the two daughter vesicles have opposite bilayer asymmetries as indicated in Fig. 5d.

Different views of closed membrane necks. Closed membrane necks look quite different when we look at them with nanoscale and mesoscale resolution. These two different views are displayed in

²In [11], the neck of an out-bud is viewed as an ‘interior neck’ because it is filled with the interior solution. Likewise, the neck of an in-bud is viewed as an ‘exterior neck’ because it is filled with exterior solution.

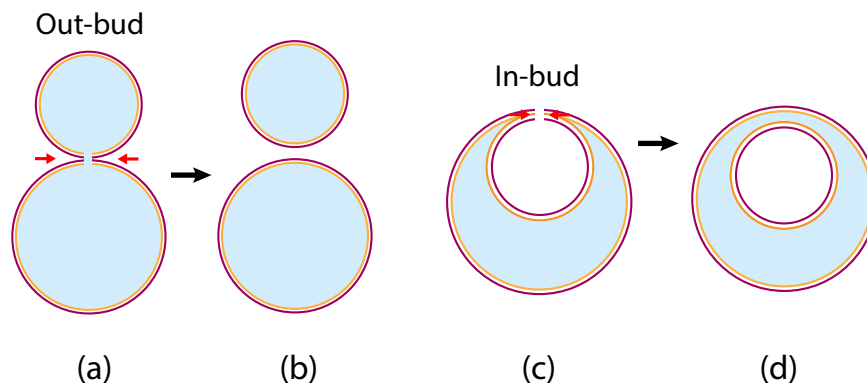


Figure 5: Fission of genus-0 vesicles by the formation and cleavage of membrane necks:: (a) Out-budded vesicle, which is formed when the membrane has a sufficiently large positive spontaneous curvature. The closed membrane neck between the out-bud and the vesicle is compressed by a curvature-dependent constriction force (red arrows); (b) The constriction force can cleave the neck, thereby dividing the out-budded vesicle into two daughter vesicles, which both have the same transbilayer asymmetry as the original genus-0 vesicle before division. The out-budded vesicle in (a) has Euler characteristic $\chi = 2$ and genus $\mathbf{g} = 0$, the two daughter vesicles in (b) have $\chi = 4$ and $\mathbf{g} = -1$; (c) In-budded vesicle, which is formed when the membrane has a sufficiently large negative spontaneous curvature. The closed membrane neck between the in-bud and the vesicle is again compressed by a curvature-dependent constriction force (red arrows); and (d) Neck cleavage now leads to two nested daughter vesicles with opposite transbilayer asymmetries. The in-budded vesicle in (c) has $\chi = 2$ and $\mathbf{g} = 0$, the two nested daughter vesicles in (d) are characterized by $\chi = 4$ and $\mathbf{g} = -1$.

Fig. 6. In panels a and b of this figure, we see a closed membrane neck at the nanoscale, as observed in molecular dynamics simulations. The lipid bilayer has a thickness of about 4 nm and forms a neck with an hourglass shape. The neck is axisymmetric and has a circular waistline. For a closed neck, the outer radius of this waistline is equal to twice the bilayer thickness whereas the inner radius vanishes. For the examples shown in Fig. 6a,b, the vesicle size is about 36 nm, which is the radius of the spherical vesicles that we would obtain from the dumbbell-shaped vesicles by osmotic inflation. Inspection of the simulation snapshots shows that the hourglass-shaped neck is highly curved in the sense that its contour curvature is large and negative whereas its other principal curvature is equal to $+1/R_{\text{ne}}$ which diverges as the neck radius R_{ne} vanishes during neck closure.

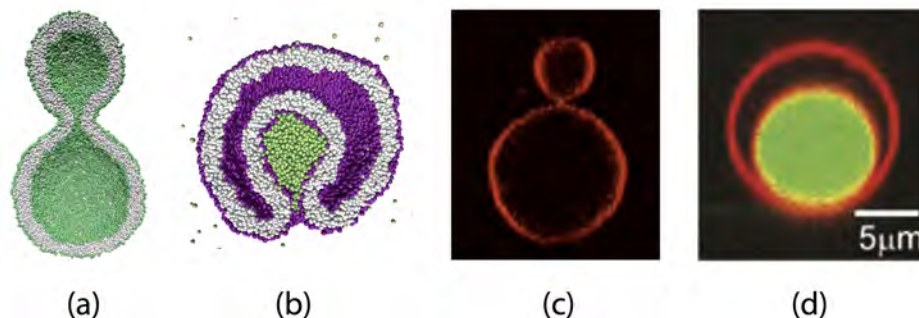


Figure 6: Closed membrane necks on nanoscopic and micrometer scales: (a,b) Hourglass shapes of closed necks on the nano scale, visualized *via* molecular dynamics simulations of nanovesicles with an out-bud in (a) [12] and an in-bud in (b) [10]; and (c,d) On the micrometer scale, closed necks appear to be pointlike as observed by fluorescence microscopy of giant unilamellar vesicles (GUVs) with fluorescently labeled lipids (red) with an out-bud in (c) [13] and an in-bud in (d) [14]. In both (b) and (d), the membrane segment of the in-bud encloses a condensate droplet (green).

At the micrometer scale, the view of the membrane neck as obtained *via* light microscopy is quite different, see panels c and d of Fig. 6. Indeed, when observed under the light microscope, the hourglass-shaped membrane segment is no longer visible but is replaced by the touching point of the two membrane segments connected by the neck. On the one hand, the pointlike neck is a direct consequence of the limited optical resolution. On the other hand, one can characterize this pointlike neck locally in terms of two important properties. First, during neck closure, the two principal curvatures diverge but the mean curvature attains a finite limit. Second, this mean curvature of the neck is directly related to the curvature radii of the two adjacent membrane segments which one can read off from the optical images. To derive these two features, we will now make a short detour into the theory of curvature elasticity.

3.2 Curvature elasticity of biomembranes

Spontaneous curvature model. In order to obtain a quantitative description of vesicle shapes with closed membrane necks, we will consider the spontaneous curvature model [15, 16, 17]. This model characterizes the membrane surface in terms of its (local) mean curvature M and its (local) Gaussian curvature G and describes the elastic curvature energy E_{cu} of the membrane by an area integral as given by

$$E_{\text{cu}} = \int dA [2\kappa(M - m)^2 + \kappa_G G] . \quad (3)$$

This expression contains three parameters, the spontaneous (or preferred) curvature m , the bending rigidity κ , and the Gaussian curvature modulus κ_G . The spontaneous curvature m provides a quantitative measure for the transbilayer asymmetry between the two leaflets of the bilayer membrane.

For a closed vesicle without membrane edges or pores, the Gauss-Bonnet theorem of differential geometry implies that the area integral over the Gaussian curvature is proportional to the Euler characteristic χ , as defined by Eq. (1), and equal to [6]

$$\int dA G = 2\pi\chi = 2\pi(2 - 2\mathfrak{g}) \quad (4)$$

with the topological genus $\mathfrak{g} = 1 - \frac{1}{2}\chi$ as in Eq. (2). For a budding process, which does not involve a topological transformation, the constant energy term proportional to the Gaussian curvature modulus κ_G can be ignored and the curvature energy reduces to the elastic bending energy

$$E_{\text{be}} = \int dA 2\kappa(M - m)^2 \quad (5)$$

which becomes small when the mean curvature M is close to the spontaneous curvature m . In order to determine the shape of a vesicle, the bending energy E_{be} has to be supplemented by constraints on the membrane area A and the vesicle volume V . At constant temperature, the membrane area A is constant, reflecting the ultralow solubility of the lipid molecules and membrane proteins. Likewise, the volume of the vesicle is conserved for constant pressure difference

$$\Delta P = P_{\text{ex}} - P_{\text{in}} \quad (6)$$

between the pressures P_{ex} and P_{in} of the exterior and interior solutions, which requires constant osmotic conditions. We are then led to minimize the vesicle's shape energy [18, 16, 17]

$$F_{\text{ve}} = \Delta P V + \Sigma A + E_{\text{be}} = \Delta P V + \Sigma A + 2\kappa \int dA (M - m)^2 \quad (7)$$

and to treat the pressure difference ΔP and the membrane tension Σ as Lagrange multipliers, which are used to perform the constrained minimization of the bending energy for a prescribed vesicle volume V and a prescribed membrane area A . Several recent studies have demonstrated that the shapes of giant vesicles calculated in this manner agree quantitatively with the experimentally observed shapes [13, 8], provided the vesicle membrane contains a molecular component such as cholesterol that undergoes frequent flip-flops from one leaflet to the other. Otherwise, one has to take area-difference-elasticity [19, 20, 21] into account which leads to a spatially non-local term in the curvature energy.

Dimensionless shape parameters. In order to reduce the number of parameters, it is convenient to define the vesicle size R_{ve} in terms of the membrane area A via

$$R_{\text{ve}} \equiv \sqrt{A/(4\pi)} \quad (8)$$

and to use R_{ve} as the basic length scale. For a closed membrane compartment with volume V and membrane area A , the shape of this compartment depends primarily on two parameters, [16] the rescaled volume

$$v \equiv \frac{V}{\frac{4\pi}{3}R_{\text{ve}}^3} = 6\sqrt{\pi} \frac{V}{A^{3/2}}, \quad (9)$$

which satisfies $0 \leq v \leq 1$, and the rescaled spontaneous curvature

$$\bar{m} \equiv mR_{\text{ve}}, \quad (10)$$

which can be positive or negative. More precisely, for each point (\bar{m}, v) , one finds a discrete set of energy branches that differ in their bending energy. For simplicity, we have tacitly assumed here that the membrane is laterally uniform with a uniform molecular composition which implies laterally uniform curvature-elastic parameters.

3.3 Stability regimes for closed membrane necks

Closed membrane necks as displayed in Fig. 5a,c exhibit large stability regimes within the two-dimensional morphology diagram, defined by the two shape parameters v and \bar{m} in Eqs. (9) and (10). These stability regimes are displayed in Fig. 7 for multispherical shapes consisting of one small and one large sphere, so-called (1+1)-multispheres. In general, vesicles can form $(N_l + N_s)$ -multispheres, consisting of N_l large and N_s small spheres. [13, 22] The multispheres represent limit shapes in the sense that they can be reached from shapes with open necks by the closure of these necks. Therefore, the multispherical shapes have the same genus, $\mathfrak{g} = 0$, as a sphere.

For (1+1)-multispheres, we have to distinguish two stability regimes depending on the sign of the spontaneous curvature. For *negative* spontaneous curvatures, the vesicles form in-buds with closed membrane necks as displayed in Fig. 5c. These in-budded shapes are stable within the light green stability regime of Fig. 7a. On the other hand, out-budded shapes as in Fig. 5a form stably closed necks in the light green stability regime of Fig. 7b which applies to *positive* spontaneous curvature.

3.4 Local stability conditions for closed necks

The stability of a closed membrane neck depends on the mean curvatures M_a and M_b of the two membrane segments adjacent to the neck. Inspection of Fig. 5 shows that the mean curvature of the mother vesicle, which we denote by M_a , is always positive. The mean curvature of the bud will be denoted by M_b . For an out- and in-bud, M_b is positive and negative, respectively. If the out- and in-budded vesicles are (1+1)-multispheres as in Fig. 5, the mean curvatures can be expressed in terms of the sphere radii R_a and R_b with $M_a = 1/R_a$ and $M_b = \pm 1/R_b$. The two mean curvatures of the membrane segments adjacent to the membrane neck define the neck curvature [7, 13]

$$M_{\text{ne}} \equiv \frac{1}{2}(M_a + M_b) = \frac{1}{2} \left(\frac{1}{R_a} \pm \frac{1}{R_b} \right) \quad (11)$$

where the first equality applies to the closed neck of any vesicle shape whereas the second equality applies to (1+1)-multispheres with the plus and minus sign for out- and in-buds. For an out-budded vesicle shape as in Fig. 5a, both M_a and M_b are positive, which implies a positive neck curvature M_{ne} . For an in-budded vesicle shape as in Fig. 5c, the membrane segment of the mother vesicle has a positive mean curvature $M_a > 0$ whereas the membrane segment of the in-bud has a negative mean curvature $M_b < 0$ with $|M_b| > M_a$. The latter inequality is necessary in order to accommodate the in-bud within the mother vesicle without intersections between the two membrane segments. As a consequence, the neck curvature M_{ne} is negative for an in-budded vesicle.

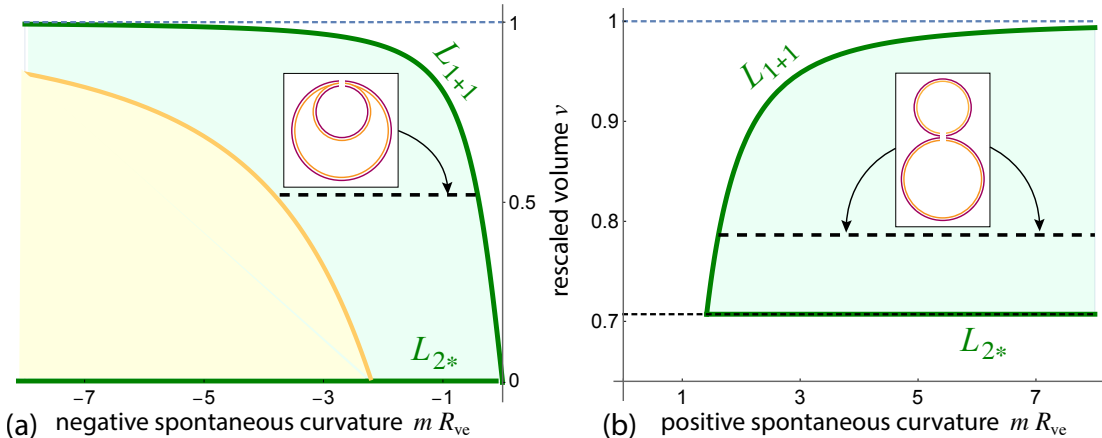


Figure 7: Stability regimes for (1+1)-multispheres with closed membrane necks: (a) For negative spontaneous curvature, stable (1+1)-shapes have in-buds, see inset and Fig. 5c; and (b) For positive spontaneous curvature, stable (1+1)-shapes exhibit out-buds, see inset and Fig. 5a. Both stability regimes (light green) are bounded by two lines of limit shapes, L_{1+1} and L_{2*} (dark green). In (a), the stability regime is also bounded by the orange line, at which the small in-budded sphere undergoes a sphere-prolate instability. Within each stability regime, the multispherical shapes are independent of the spontaneous curvature \bar{m} but depend only on the rescaled volume v as defined by Eq. (9). Thus, the (1+1)-multispherical shapes remain unchanged when \bar{m} is varied for fixed v (horizontal dashed lines). Note the different range of v -values in (a) and (b).

A closed membrane neck with positive neck curvature M_{ne} is stable if the spontaneous curvature m is *positive* and sufficiently large with [7, 17]

$$m \geq M_{\text{ne}} > 0 \quad (\text{stably closed neck for positive } m). \quad (12)$$

The limiting case with $m = M_{\text{ne}} > 0$ corresponds to the green line of limit shapes L_{1+1} in Fig. 7b, which provides one boundary for the green shaded stability regime of (1+1)-multispheres with positive spontaneous curvature. The second boundary of this stability regime, denoted by L_{2*} in Fig. 7b, corresponds to the limit shapes of two equally sized spheres. The line L_{2*} is a direct consequence of the geometry for (1+1)-spheres with out-buds. Indeed, this geometry implies that the rescaled volume v cannot be smaller than $v_2 = 1/\sqrt{2} = 0.7071$. Each line of limit shapes separates the stability region of the (1+1)-multispherical shapes from a region of the morphology diagram, in which the vesicles have a smoothly curved shape with open necks.

For a closed neck with negative neck curvature M_{ne} , the closed membrane neck is stable if the spontaneous curvature m is *negative* and has a sufficiently large absolute value with [17, 11]

$$m \leq M_{\text{ne}} \leq 0 \quad (\text{stably closed neck for negative } m). \quad (13)$$

The limiting case with $m = M_{\text{ne}} < 0$ corresponds to the green line of limit shapes L_{1+1} in Fig. 7a, which provides one boundary for the green shaded stability regime of (1+1)-multispheres with negative spontaneous curvature. The second boundary, denoted by L_{2*} in Fig. 7a, corresponds to the line of limit shapes L_{2*} , for which the in-bud has the same size as the mother vesicle. The line L_{1+1} again separates the stability regime of the (1+1)-multispheres from smoothly curved vesicle shapes with open necks. For negative spontaneous curvatures, the limit shapes L_{2*} of two equally sized spheres are located at $v = v_2 = 0$ which implies that one cannot cross this line to reach some smoothly curved vesicle shapes.

The stability relations for stably closed necks in Eqs. (12) and (13) were originally obtained from numerical calculations for axially symmetric vesicle shapes approaching the limit shapes L_{1+1} . [16] For out-budded vesicles, the stability relations were also obtained from a certain parametrization of the shape in terms of piece-wise constant-mean-curvature surfaces. [23] The stability relations for (1+1)-multispheres have been generalized to vesicles with two intramembrane domains [24] and to

non-axisymmetric vesicle shapes [25]. The limit shapes L_{2*} of two equally sized spheres follow from a detailed analysis of the multisphere geometry. [7] In addition, the stability relations for closed necks lead to constriction forces acting on these necks. These constriction forces increase with the absolute value of the spontaneous curvature and are enhanced both by the line tension of domain boundaries and by the complete engulfment of adhesive nanoparticles, see Section 3.7 below.

3.5 Geometric relation between volume and neck curvature

As mentioned, the neck curvature M_{ne} is equal to the spontaneous curvature m along the two lines of limit shapes L_{1+1} in the two panels of Fig. 7. For these two lines, one can obtain an explicit expression for the volume v as a function of the spontaneous curvature m in the (\bar{m}, v) morphology diagram. [16, 17] Substituting the rescaled spontaneous curvature \bar{m} by the rescaled neck curvature

$$\bar{M}_{\text{ne}} \equiv M_{\text{ne}} R_{\text{ve}} = \frac{1}{2} \left(\frac{R_{\text{ve}}}{R_a} \pm \frac{R_{\text{ve}}}{R_b} \right), \quad (14)$$

one obtains the explicit relationship

$$v = v_{1+1}(x) \equiv -\frac{1}{4x^3} + \left(1 - \frac{1}{2x^2}\right) \sqrt{1 + \frac{1}{4x^2}} \quad \text{with} \quad x \equiv \bar{M}_{\text{ne}} \quad (15)$$

between the rescaled volume v and the rescaled neck curvature \bar{M}_{ne} . The purely geometric relationship in Eq. (15) applies both to the first branch of limit shapes L_{1+1} with negative spontaneous curvature in Fig. 7a and to the second branch of L_{1+1} with positive spontaneous curvature in Fig. 7b. Furthermore, inspection of panels a and b of Fig. 7 shows that the volume $v = v_{1+1}(\bar{M}_{\text{ne}})$ as given by the relationship in Eq. (15) increases monotonically for increasing positive $\bar{M}_{\text{ne}} \geq \sqrt{2}$ and for decreasing negative $\bar{M}_{\text{ne}} \leq 0$. This monotonicity implies that the functional relation in Eq. (15) can be inverted to obtain the neck curvature \bar{M}_{ne} as a function of v for both branches of limit shapes L_{1+1} .

3.6 Emergence of closed neck conditions

Next, we will discuss the closure of the membrane neck in more detail, starting from the hourglass-shaped neck in panels a and b of Fig. 6 as observed on the nanoscale. In these simulation snapshots, the waistline (wl) of the neck forms a circle with radius R_{ne} . Along this waistline, the neck is characterized by two principal curvatures, the negative contour curvature $C_{1,\text{wl}} < 0$ perpendicular to the waistline and the positive principal curvature $C_{2,\text{wl}} = 1/R_{\text{ne}} > 0$ parallel to the waistline. When the neck closes, the neck radius goes to zero and the principal curvature $C_{2,\text{wl}}$ diverges. However, the mean curvature

$$M_{\text{wl}} = \frac{1}{2} (C_{1,\text{wl}} + C_{2,\text{wl}})$$

remains finite and satisfies the asymptotic equality

$$M_{\text{wl}} \approx M_{\text{ne}} \equiv \frac{1}{2} (M_a + M_b) \quad (16)$$

in the limit of small R_{ne} , [26] with the mean curvature M_{ne} of the closed neck determined by the mean curvatures M_a and M_b of the two membrane segments, a and b , adjacent to the neck. Thus, as the neck closes, the positive singular contribution from the second principal curvature $C_{2,\text{wl}} = 1/R_{\text{ne}} > 0$ is cancelled by a negative contribution arising from the contour curvature $C_{1,\text{wl}}$. Therefore, neck closure involves a singular catenoid with vanishing mean curvature that does not contribute to the mean curvature of the membrane neck. After the cancellation of the two singular contributions, we are left with the neck curvature M_{ne} as given by Eq. (16), which is positive for out-buds with $M_a > 0$ and $M_b > 0$ but negative for in-buds with $M_a > 0$ and $M_b < -M_a < 0$.

3.7 Constriction forces at closed membrane necks

Curvature-induced constriction forces. As mentioned, the shape of a (1+1)-multisphere depends only on the rescaled volume v and, thus, does not change when we vary the spontaneous

curvature \bar{m} within the stability regimes, see horizontal dashed lines in Fig. 6. However, this variation leads to a change in the constriction force acting at the membrane neck. Indeed, the closed membrane necks displayed in panels a and c of Fig. 5 can experience significant constriction forces, f , that increase with the absolute value of the spontaneous curvature. These constriction forces have the form [7, 8]

$$f \approx 8\pi\kappa(m - M_{\text{ne}}) \quad \text{for } 0 < M_{\text{ne}} \leq m \quad (17)$$

and

$$f \approx 8\pi\kappa(M_{\text{ne}} - m) \quad \text{for } m \leq M_{\text{ne}} \leq 0, \quad (18)$$

where the asymptotic equalities are valid to leading order in the neck radius R_{ne} . These constriction forces vanish along the line of limit shapes, L_{1+1} , for which the neck curvature M_{ne} is equal to the spontaneous curvature m . Furthermore, as we vary the spontaneous curvature, the constriction force is proportional to the excess curvature $m - M_{\text{ne}}$ for $m > 0$ and to the excess curvature $M_{\text{ne}} - m$ for $m < 0$.

The constriction forces in Eqs. (17) and (18) can be obtained in a simple and direct manner starting from the bending energy E_{be} of a dumbbell shape with an open neck of radius R_{ne} which has the form [7]

$$E_{\text{be}}(R_{\text{ne}}) \approx E_{\text{be}}(0) \pm 8\pi\kappa(m - M_{\text{ne}})R_{\text{ne}} \quad (19)$$

up to first order in R_{ne} where the plus and minus sign applies to positive and negative spontaneous curvature, respectively. The constriction force f compressing the membrane neck is then given by

$$f = \partial E_{\text{be}} / \partial R_{\text{ne}}, \quad (20)$$

which leads to Eqs. (17) and (18) depending on the sign in Eq. (19). In both cases, the force depends only on local properties of the membrane segments close to the neck. Therefore, the constriction forces in Eqs. (17) and (18) are not restricted to the necks of out- and in-buds but apply to any neck with $m \geq M_{\text{ne}} > 0$ and to any neck with $m \leq M_{\text{ne}} \leq 0$, respectively. In particular, these constriction forces apply to the necks of multispheres to be considered in Section 6 below.

When we look at a closed neck with molecular resolution as in panels a and b of Fig. 6, we see that the membrane neck is formed by two bilayer segments in close contact and that the neck diameter is about twice the bilayer thickness. For an open neck, the two bilayer segments are fully hydrated and each bilayer has a thickness of 4 to 5 nm, depending on the chain length of the lipid molecules. This bilayer thickness will persist until neck closure with $m = M_{\text{ne}}$ and vanishing constriction force, $f = 0$, but will start to decrease for $m > M_{\text{ne}}$ when the two segments are pushed together by a positive constriction force, $f > 0$. In the latter case, the constriction force is balanced by an elastic counter force arising from the locally compressed bilayer segments.

Magnitude of curvature-induced constriction forces. As an example, let us consider a GUV enclosed by a lipid membrane with positive spontaneous curvature and bending rigidity $\kappa = 48 k_{\text{B}}T$, as studied experimentally in [8], see Section 4.1 below. The corresponding curvature-induced constriction force f is depicted in Fig. 8a and plotted in Fig. 8b as a function of the excess curvature $m - M_{\text{ne}}$. For comparison, this plot also includes literature values for constriction forces as generated by specialized protein complexes *in vivo*. Inspection of Fig. 8b reveals that the constriction force acting on the closed neck of the giant vesicle in Fig. 8a lies within the range of constriction forces generated by proteins *in vivo*.

Constriction forces enhanced by line tension of domain boundaries. The curvature-induced constriction force is enhanced if the neck contains a domain boundary between two membrane domains a and b that differ in their molecular composition. The line tension λ_{db} of the domain boundary must be positive to ensure that the domains are thermodynamically stable. If the two membrane domains have comparable curvature-elastic properties, the constriction force is given by [11]

$$f \approx 8\pi\kappa(m - M_{\text{ne}}) + 2\pi\lambda_{\text{db}} \quad \text{for } 0 < M_{\text{ne}} \leq m + \lambda/(4\kappa) \quad (21)$$

and by

$$f \approx 8\pi\kappa(M_{\text{ne}} - m) + 2\pi\lambda_{\text{db}} \quad \text{for } 0 \geq M_{\text{ne}} \geq m - \lambda/(4\kappa). \quad (22)$$

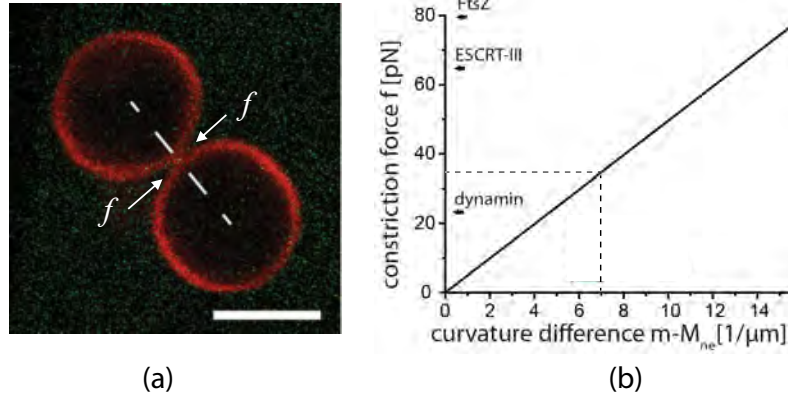


Figure 8: Curvature-induced constriction force f at closed membrane neck: (a) Confocal image of a GUV membrane (red) that consists of two equally sized spheres connected by a closed neck. The spontaneous curvature is generated by His-tagged GFP which binds to the membrane from the exterior solution. The constriction force f (white arrows) acts to compress this neck. Scale bar: $5 \mu\text{m}$; and (b) Constriction force f as a function of the excess curvature $m - M_{\text{ne}}$. The straight line corresponds to Eq. (17) with $\kappa = 48 k_{\text{B}}T$. The dashed lines represent the values of $m - M_{\text{ne}}$ and f for the membrane neck in (a). For comparison, the plot also includes literature values for the constriction forces as generated by the specialized protein complexes of dynamin [27], ESCRT-III [28], and FtsZ [29]. Thus, the constriction force in (a) lies within the range of force values found *in vivo*. [8]

Therefore, the line tension λ_{db} of the domain boundary enhances the constriction force f at the closed neck for both out-budded and in-budded vesicles. In both cases, the neck curvature M_{ne} is again a purely geometric quantity, compare Section 3.5 above, whereas the spontaneous curvature m and the line tension λ_{db} are material parameters.

In general, the two membrane domains a and b may have different curvature-elastic properties. The corresponding constriction forces are obtained from Eqs. (21) and (22) by replacing the terms $\pm 8\pi\kappa(m - M_{\text{ne}})$ by $\pm 4\pi[\kappa_a(m_a - M_a) + \kappa_b(m_b - M_b)]$ while the line tension terms remain unchanged. [11]

Constriction forces enhanced by adhesion. The constriction forces are also enhanced by the engulfment of adhesive nanoparticles. The competition between the adhesion energy per unit area, W , and the bending rigidity κ is encoded in the adhesion length [30, 31]

$$R_W = \sqrt{2\kappa/|W|} \quad (23)$$

If the adhesive particle is completely engulfed by an out-bud, which initiates the process of particle exocytosis, the constriction force f has the form [32]

$$f \approx 8\pi\kappa(m - M_{\text{ne}}) + \frac{4\pi\kappa}{R_W} = 8\pi\kappa \left(m - M_{\text{ne}} + \frac{1}{2R_W} \right) \quad (24)$$

which implies

$$f \geq 0 \quad \text{for} \quad 0 < M_{\text{ne}} \leq m + \frac{1}{2R_W} = m + \sqrt{\frac{|W|}{8\kappa}} \quad (25)$$

On the other hand, if the adhesive particle is completely engulfed by an in-bud, the first step during particle endocytosis, the constriction force is given by [32]

$$f \approx 8\pi\kappa(M_{\text{ne}} - m) + \frac{4\pi\kappa}{R_W} = 8\pi\kappa \left(M_{\text{ne}} - m + \frac{1}{2R_W} \right) \quad (26)$$

which implies

$$f \geq 0 \quad \text{for} \quad 0 \geq M_{\text{ne}} \geq m - \frac{1}{2R_W} = m - \sqrt{\frac{|W|}{8\kappa}}. \quad (27)$$

Therefore, the complete engulfment of an adhesive nanoparticle leads to an increase of the constriction force f at the closed neck by

$$\Delta f = \frac{4\pi\kappa}{R_W} = 2\pi\sqrt{2\kappa|W|} \quad (28)$$

for both out-budded and in-budded vesicles. This adhesion-induced enhancement of the constriction force agrees with the intuitive notion that it will be more difficult to open the neck when it is stabilized by adhesion.

The adhesion-induced enhancement of the constriction force has been derived for the engulfment of spherical nanoparticles, which are solid, have a fixed shape, and cannot be deformed by the membrane. Strictly speaking, the latter constraint does not apply to the engulfment of condensate droplets. On the other hand, when these droplets are completely engulfed as in Figs. 6b and 6d, they usually attain a spherical shape. In this case, the adhesion-induced enhancement of the constriction force is expected to apply to liquid droplets as well, provided we identify the parameter W with the affinity contrast between the two aqueous phases [33].

Large constriction forces drive fission. We now consider an out-budded or in-budded vesicle with a closed membrane neck and increase the absolute value of the spontaneous curvature \bar{m} , thereby moving along one of the horizontal dashed lines in Fig. 7. When we increase the absolute value $|\bar{m}|$, the shape of the (1+1)-vesicle remains unchanged but the constriction forces as described by Eqs. (17) – (24) increase. A sufficiently large constriction force acting on an individual membrane neck leads to the fission of this neck and to the division of the vesicle. Such fission processes have been recently observed for several biomimetic membrane systems as will be described in Section 4 below.

3.8 Free energy landscape for fission

The fission process involves the closure and subsequent cleavage of a membrane neck, as shown schematically in Fig. 9a-c, where we display the fission of a small nanovesicle in order to explicitly resolve the lipid bilayer. The neck cleavage has to overcome a free energy barrier arising from the local disruption of the bilayer structure. On the supramolecular scale, one may envisage this barrier for neck fission to arise from a cut across the bilayer and the creation of two ring-like hydrophobic bilayer edges across the neck. The ‘healing’ of these bilayer edges then leads to two separate daughter vesicles. Furthermore, the energy barrier associated with fission is proportional to the total length of the bilayer edges, which is minimal if the bilayer is cut across the neck.

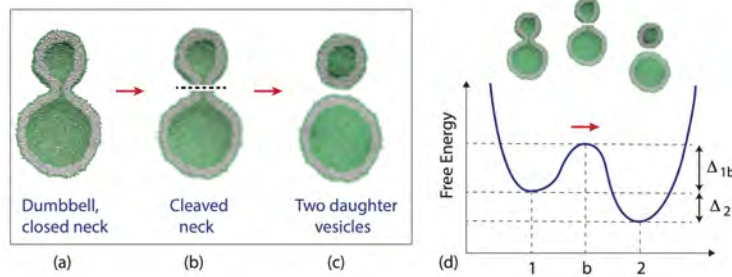


Figure 9: Fission of small nanovesicle and corresponding free energy landscape: (a-c) Schematic fission process which starts from a dumbbell with a closed neck in (a), proceeds via the cleavage of this neck in (b), corresponding to the shortest possible cut (broken line) across the vesicle membrane, and ends up with two separate daughter vesicles in (c). The cut leads to two circular membrane edges which have a positive line tension and determine the free energy barrier; and (d) Schematic free energy landscape versus an abstract reaction coordinate, with the free energy barrier provided by the cleaved neck. For the fission process to be ‘downhill’ (exergonic) in free energy, the free energy difference Δ_{21} between the two vesicle state 2 and the dumbbell state 1 must be negative. For $\Delta_{21} < 0$, the fission process can proceed without being coupled to another process such as nucleotide hydrolysis but the fission rate is determined by the positive free energy barrier Δ_{1b} .

A cut across the neck creates two bilayer pores with a diameter that is comparable to the size of the closed membrane neck before fission. The resulting free energy barrier is governed by the edges of these two pores and the associated edge energy, which is equal to the edge tension λ_{ed} times the combined circumference of the two pores. To lower this barrier by a significant amount, the constriction force f in Eq. (17) must perform mechanical work that is comparable to the edge energy. [7, 17] One then finds that the neck undergoes fission if the spontaneous curvature m exceeds the threshold value $m_* \equiv \lambda/(2\kappa)$. This threshold value is reduced if the neck contains a domain boundary between two intramembrane domains, see Eqs. (21) and (22), or if the membrane segment adjacent to the neck contains an adhesive particle or droplet, see Eqs. (24) and (26).

The process displayed in Fig. 9 represents a topological transformation from a single vesicle to two separate daughter vesicles. Both states have essentially the same bending energy because the bending energy of the closed neck is proportional to its area which is much smaller than the total membrane area of the vesicle. However, the two states have different topologies which implies that the Gaussian curvature term in Eq. (3) makes a different contribution to the one- and two-vesicle states. The latter contribution is equal to $4\pi\kappa_G$ for the one-vesicle state and to $8\pi\kappa_G$ for the two-vesicle state, where κ_G is the Gaussian curvature modulus. Therefore, the difference in free energy, $G_2 - G_1$, between the two- and the one-vesicle state is equal to $4\pi\kappa_G$.

Both experimental studies [34, 35] and computer simulations [36] indicate that the Gaussian curvature modulus is negative with $\kappa_G \simeq -\kappa$. For the lipid membranes studied here, we then obtain the estimate $\kappa_G \simeq -48k_B T$ which leads to the free energy difference $G_2 - G_1 \simeq -603k_B T$. Therefore, neck fission and GUV division is a strongly exergonic process and can, in principle, occur spontaneously. However, the rate with which this process proceeds is governed by the free energy barrier that separates the one-vesicle from the two-vesicle state.

3.9 Contact lines with positive and negative line tensions

In the previous subsections, we implicitly assumed that the closure of a membrane neck proceeds in an axisymmetric manner. This assumption applies to the neck closure of GUV membranes with a uniform composition as in Fig. 8. The same assumption also applies to domain-induced budding of vesicle membranes, for which the membrane neck contains the domain boundary between two different membrane domains, a and b . As mentioned, the line tension λ_{db} of such a domain boundary is always positive which implies that this boundary prefers to attain a circular shape. On the other hand, the assumption about axisymmetry is less obvious for the engulfment of condensate droplets because the line tension of the contact line between membrane and droplets is not necessarily positive but can be negative as well.

Indeed, strongly non-axisymmetric membrane necks have been observed in molecular dynamics simulations for the engulfment of condensate droplets by planar [37] and by vesicle [10] bilayers. In both cases, the contact line between droplet and membrane becomes strongly non-circular, which reveals a *negative* line tension. As a consequence, the membrane neck close to the contact line attains an unusual, tight-lipped shape. Such a tight-lipped neck has also been observed for the membrane engulfment of solid and undeformable nanoparticles by planar bilayers. [38] A tight-lipped membrane neck prevents the fission of the neck and, thus, the division of the vesicle.

For a contact line between condensate droplet and membrane, the sign of the line tension is controlled by the initial stress asymmetry $\Delta\Sigma = \Sigma_1 - \Sigma_2$ between the two leaflet tensions, Σ_1 and Σ_2 , of the two leaflets, as measured in the absence of the droplet [10, 38] A relatively small stress asymmetry leads to a negative line tension and a tight-lipped membrane neck, which does not undergo fission, whereas a sufficiently large stress asymmetry leads to a positive line tension, which ensures that neck closure proceeds in an axisymmetric manner and that the closed neck undergoes fission. [10, 38]

4 Fission of Biomimetic Membranes

4.1 Division of giant unilamellar vesicles

A particularly amazing property of living cells is their ability to divide into two daughter cells. During cell division, the plasma membrane undergoes a series of morphological transformations which ultimately lead to membrane fission. Analogous remodeling processes have been induced by low densities of proteins bound to the membranes of GUVs. [8] When these proteins are fluorescently labeled and bound to the membranes via histidine-tags and anchor lipids, an unprecedented control over the spontaneous curvature has been achieved. In fact, the spontaneous curvature can be directly controlled by the molar concentration of the histidine-tagged proteins in the exterior solution. Fine-tuning of this curvature leads to dumbbell-shaped vesicles with closed membrane necks as in Fig. 8a. Because the proteins bind to the outer leaflet of the GUV membranes, the induced spontaneous curvature is positive and generates a significant constriction force, see Fig. 8b., that is sufficient to cleave the neck and divide the GUV as illustrated in Fig. 10 using green fluorescent protein (GFP). These experiments confirm the curvature-induced constriction force as described by Eq. (17) in a quantitative manner.

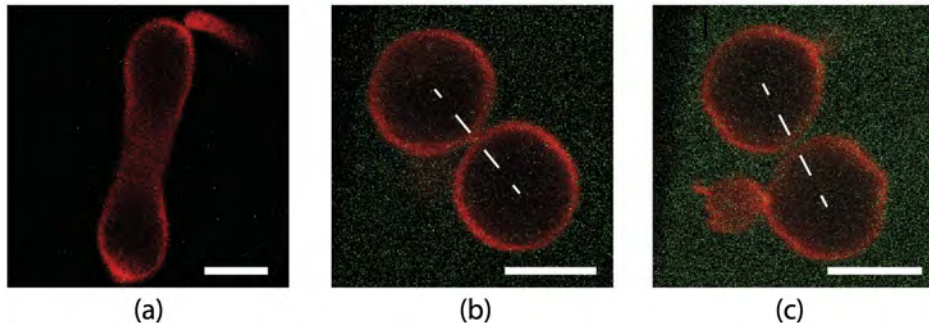


Figure 10: Curvature-induced division of a GUV: (a) Dumbbell-shaped vesicle obtained by osmotic deflation; (b) When green fluorescent protein (GFP) is added to the exterior solution, the vesicle attains a two-sphere shape with a closed neck. The GFP binds to anchor lipids in the outer leaflet of the GUV membrane, generating a positive spontaneous curvature as well as a substantial constriction force compressing the neck; and (c) Increasing the spontaneous curvature by adding more GFP, the membrane neck is cleaved and the GUV is divided into two daughter vesicles, even though the GFP concentration is still very low and only 39 nM. All scale bars: 5 μm . [8]

The division of GUVs as illustrated in Fig. 10 involves two key parameters, the (rescaled) spontaneous curvature \bar{m} and the (rescaled) vesicle volume v . The spontaneous curvature is controlled by adding histidine-tagged proteins to the exterior solution of the GUVs. The vesicle volume can be directly controlled by the osmotic conditions. For a sufficiently small volume, a dumbbell shape is reached as in Fig. 10a. Increasing the spontaneous curvature of the GUV membrane by adding GFP to the exterior solution then leads to the two-sphere shape with a closed neck as displayed in Fig. 10b. This shape is close to the line of limit shapes L_{2*} in Fig. 7b. Adding more GTP, we move along this line towards larger values of the spontaneous curvature, eventually reaching a sufficiently large constriction force that cleaves the neck. It is important to note that neck fission and vesicle division are obtained for very low GTP concentrations in the nanomolar regime. The membrane neck in Fig. 10b, for example, was cleaved for a GTP concentration of only 39 nM.

Comparison with alternative experimental approaches. Other experimental approaches have been pursued in order to achieve the division of lipid vesicles. [39, 40, 41, 42, 43, 26, 44] In what follows, these alternative approaches will be briefly summarized. First, PEG-dextran solutions within a GUV undergo aqueous phase separation into a PEG-rich and a dextran-rich droplet. The GUV membrane enclosing these two droplets can form a closed membrane neck in between the two droplets, thereby partitioning the membrane into two segments in contact with the PEG-rich and dextran-rich phase. [39] However, these two membrane segments remained connected by a membrane nanotube (or

‘tether’), which prevented their genuine division. Another approach was based on the reconstitution of the bacterial division machinery provided by FtsZ proteins. The formation of relatively large rings of these proteins within GUVs has been observed, albeit with rather low frequency. [40] For about 1.2 percent of the GUVs, protein rings were observed to induce progressive constrictions of the GUVs, in some cases leading to two subcompartments connected by closed membrane necks. However, the subsequent division into two separate membrane compartments has not been reported. Furthermore, the buffer used in this latter approach involved two nucleotides, ATP and GTP. In the absence of GTP, no progressive constrictions of GUVs could be detected.

In Ref. [41], extruded vesicles with a diameter of 200 nm were exposed to histidine-tagged GFP. The vesicle membranes contained 20 mol% anchor-lipids and were exposed to a GFP solution concentration of 5 and 20 μM . As a consequence, the anchor-lipid mole fraction was at least 20 times higher and the GFP solution concentration was at least 128 times larger compared to the GUV system described by us in [8] and displayed in Fig. 10. In fact, it was concluded in Ref. [41] that crowding of membrane-bound GFP is a prerequisite for successful vesicle division. In contrast, our results clearly demonstrate that vesicle division can be achieved by membrane-bound proteins in the dilute regime, in which the separation of the membrane-bound proteins is much larger than their lateral size.

A microfluidic-based approach was used in Ref. [42] to mechanically split GUVs into two daughter vesicles. The GUVs were formed from double-emulsion droplets and subsequently flowed against the sharp edge of a wedge-shaped microfluidic junction. The resulting division process competed primarily with two alternative outcomes, bursting of the GUV and futile division attempts with no splitting (called ‘snaking’ in Ref. [42]). As a consequence, the probability for division was observed to depend strongly on the size of the GUV and to follow a bell-shaped curve with a maximum at a GUV diameter of about 6 μm . For the latter size, the division probability was about 0.38. Both for smaller and for larger sizes, the division probability decreased rapidly to zero: For smaller sizes, futile division attempts became the typical outcomes whereas larger GUVs were destroyed by bursting. In contrast, our approach (Figs. 8 and 10) should be size-independent because the curvature-induced constriction force as given by Eq. (17) compresses the neck locally and does not involve the size of the GUV.

GUVs enclosing Min proteins undergo shape oscillations [43], during which the vesicles change their neck size in a recurrent manner [26]. These oscillations are driven by the Min proteins that bind to and unbind from the vesicle membrane [45], with the detachment being controlled by the ATP hydrolysis. The observed shape oscillations can be understood in terms of a spontaneous curvature that undergoes cyclic changes in time. [26] During each oscillation cycle, the vesicle shape is transformed from a symmetric dumbbell with two equally sized subcompartments to an asymmetric dumbbell with two subcompartments that differ in their size, followed by the reverse, symmetry-restoring transformation.

As previously mentioned, see Eq. (21), the constriction force compressing the membrane neck can be enhanced by the line tension λ_{db} of a domain-boundary between two membrane domains when this boundary is located at the membrane neck. Thus, the presence of such a domain boundary should facilitate the fission of the neck. The latter process may have been observed in Ref. [44] but the published optical images make it difficult to decide whether or not the two membrane segments remain connected by a membrane nanotube as in Ref. [39].

4.2 Division of unilamellar nanovesicles

Division via large transbilayer asymmetry. In molecular dynamics simulations, the transbilayer asymmetry of vesicle bilayers can be directly controlled by the number of lipids, N_{il} and N_{ol} , which are assembled in the inner and outer leaflet of the vesicle bilayer. Instead of the lipid numbers, which are extensive variables, one can consider the leaflet tensions Σ_{il} and Σ_{ol} of the inner and outer leaflets, which represent intensive variables. The sum of the two leaflet tensions is equal to the bilayer tension, $\Sigma = \Sigma_{ol} + \Sigma_{il}$. The stress asymmetry between the two leaflets of the vesicle bilayer is given by [46, 10, 38]

$$\Delta\Sigma = \Sigma_{ol} - \Sigma_{il}, \quad (29)$$

which vanishes for symmetric bilayer states with $\Sigma_{ol} = \Sigma_{il}$. On the other hand, the leaflets of tensionless bilayers with vanishing bilayer tension, $\Sigma = \Sigma_{ol} + \Sigma_{il} = 0$, experience opposite leaflet tensions, $\Sigma_{il} = -\Sigma_{ol}$, corresponding to one stretched and one compressed leaflet. One particularly important bilayer state is provided by the reference state with tensionless leaflets and $\Sigma_{ol} = \Sigma_{il} = 0$.

In our first nanovesicle simulations [12], we focussed on nanovesicles, which were assembled from a fixed total number of $N_{ol} + N_{il} = 10100$ lipids in both leaflets, and varied the lipid number N_{ol} in the outer leaflet from $N_{ol} = 5700$ to $N_{ol} = 6300$. These vesicles have a radius of $22d$ where $d \simeq 0.8$ nm is the basic length scale used to parametrize the coarse-grained molecular model. For $N_{ol} = 5700$ and $N_{il} = 4400$, the spherical vesicles with tensionless bilayers experience the stress asymmetry $\Delta\Sigma = 1.69\gamma$, with the tension scale $\gamma \equiv k_B T/d^2$, which has the value $\gamma \simeq 6.4$ mN/m at room temperature. Starting with such a spherical vesicle, a reduction of the vesicle volume creates an in-budded vesicle with an open neck. [12] When the lipid number N_{ol} in the outer leaflet is further reduced to $N_{ol} = 5500$, the stress asymmetry of the tensionless bilayer is increased to $\Delta\Sigma = 2.67\gamma$. For the latter stress asymmetry, the reduction of the vesicle volume leads to an in-bud with a closed neck that undergoes fission, see Fig. 11.



Figure 11: Time-lapse snapshots for the division of a nanovesicle with $N_{ol} = 5500$ lipids in the outer and $N_{il} = 4600$ lipids in the inner leaflet. Until time $t = 0 \mu\text{s}$, the vesicle has a spherical shape with a certain volume as determined by the number of water molecules within the interior vesicle compartment. At $t = 0 \mu\text{s}$, the vesicle volume is reduced by 20 percent. After this volume reduction, the vesicle develops an in-bud with a membrane neck that is closed at $t = 5 \mu\text{s}$. At about $t = 15 \mu\text{s}$, the neck undergoes fission, thereby generating an intraluminal daughter vesicle that adheres to the inner leaflet of the larger daughter vesicle. [38]

Nanovesicle division via solute adsorption. Budding and fission of nanovesicles can also be induced by the adsorption of small solutes onto the vesicle membranes. [9] We used an off-lattice model for a binary mixture consisting of water and solute beads and studied this model by molecular dynamics simulations. In Ref. [9], we focussed on low solute concentrations and on the one-phase region of the binary mixture, in which the solutes formed adsorption layers on the outer leaflet of the vesicle membranes. This adsorption generated a significant spontaneous curvature that could be used to change the morphology of the vesicles.³ In addition to the solute concentration, we identified the solvent conditions as a second key parameter for these processes. By definition, good solvent conditions imply that the solution remains spatially uniform for all solute concentrations. A poor solvent, on the other hand, leads to a certain range of solute concentrations in which the solution undergoes liquid-liquid phase separation. Examples for this kind of phase behavior are provided by aqueous two-phase systems [47, 48, 49], by water-in-water emulsions [50], and by biomolecular condensates [51, 52].

For *good* solvent conditions, the budding of a nanovesicle can be controlled by reducing the vesicle volume for constant solute concentration or by increasing the solute concentration for constant vesicle volume. After the budding process has been completed, the budded vesicle consists of two membrane subcompartments which are connected by a closed membrane neck. The budding process is reversible as can be demonstrated explicitly by reopening the closed neck via a decrease of the solute concentration. For *poor* solvent conditions, on the other hand, we observed two unexpected morphological transformations of the nanovesicles, as shown by the simulation snapshots in Fig. 12. Close to the binodal line, at which the aqueous solution undergoes phase separation, the vesicle exhibits recurrent shape changes with closed and open membrane necks, see the simulation snapshots in Fig. 12 a, which cover a time period of about $35 \mu\text{s}$ and are reminiscent of the flickering fusion pores (kiss-and-run) that have been observed for synaptic vesicles [53, 54, 55].

³In [9], the solute molecules were contained in the exterior solution and their adsorption onto the outer vesicle leaflet generated a positive spontaneous curvature. A negative spontaneous curvature is obtained when the solutes are adsorbed from the interior solution onto the inner vesicle leaflet.

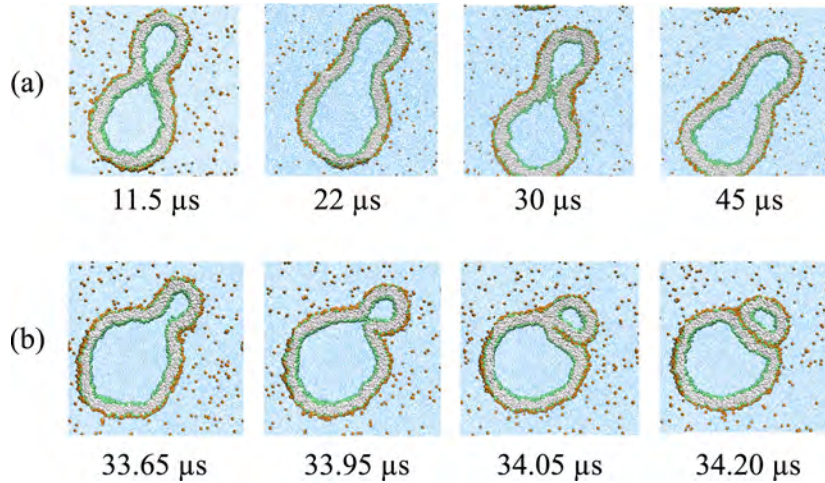


Figure 12: Unusual morphological transitions of nanovesicles exposed to small solutes (orange dots) in the exterior aqueous solution (blue), for low solute concentrations Φ and poor solvent conditions. The nanovesicles have a size of about 36 nm. The cross-sections of the vesicle membranes depict lipid bilayers with green head groups and grey hydrocarbon chains. The solutes form adsorption layers (orange-green) at the outer leaflets of the bilayers: (a) Time series of budded nanovesicle with recurrent shape changes between dumbbells with open and closed necks for solute mole fraction $\Phi = 0.025$; and (ii) Division of nanovesicle by fission of the membrane neck for $\Phi = 0.026$, which leads to two daughter vesicles that adhere via the adsorbed solutes. Both mole fractions belong to the one-phase region but are located close to the binodal line. [9]

As we approach the binodal line even closer, the recurrent shape changes are truncated by the fission of the membrane neck which leads to the division of the nanovesicle into two daughter vesicles, see the simulation snapshots in Fig. 12b, which cover a relatively short time period of less than a microsecond and show the last neck closure and the subsequent fission event. Inspection of Fig. 12b and the associated time-lapse movie reveals that the underlying fission mechanism is provided by the solute-mediated adhesion of the two membrane segments close to the neck, which leads to a growing, non-axisymmetric contact area between these two segments. In this way, our simulations reveal a nanoscale mechanism for the budding and fission of nanovesicles, a mechanism that arises from the interplay between membrane elasticity and solute-mediated membrane adhesion.

Other simulation studies of nanovesicle fission. Fission of nanovesicles has also been observed in other simulation studies. When a solid nanoparticle is completely engulfed by the vesicle membrane, a neck is formed that may undergo fission as observed in Brownian dynamics simulations without explicit water. [56] This process is governed by the adhesion between the membrane and the nanoparticle, which leads to the adhesion-dependent constriction force described by Eq. (24). [31, 32] Fission has also been observed in coarse-grained molecular simulations of bilayers with two lipid components [57, 58] and in dissipative particle dynamics of monolayers assembled from triblock copolymers [59]. The nanovesicle in Ref. [57] was formed by an asymmetric bilayer exposed to two different types of water beads in the interior and exterior compartment. The associated spontaneous curvature generates a constriction force that can be sufficiently large to cleave the neck, in analogy to the experimentally observed behavior of giant vesicles [8] displayed in Figs. 8 and 10. The latter mechanism also applies to the fission of one-component monolayers of asymmetric block copolymers. [59] The two-component bilayers and monolayers in Refs. [58] and [59] consisted of two membrane domains with the domain boundary being located within the membrane neck of the dumbbell-shaped vesicles. In such a situation, the cleavage of the neck depends both on the spontaneous curvature and on the line tension λ_{db} of the domain boundary, see Eq. (21). Furthermore, using coarse-grained molecular models, the cleavage of membrane necks by protein helices mimicking dynamin has also been studied by simulations in Ref. [60].

4.3 Endocytosis of condensate droplets

Condensate droplets are formed in aqueous solutions of macromolecules that undergo phase separation into two liquid phases. [33] A well-studied example are solutions of the two polymers PEG and dextran which have been used for a long time in biochemical analysis and biotechnology. [47, 50] More recently, phase separation has also been observed in living cells where it leads to membrane-less or droplet-like organelles. In the latter case, the condensate droplets are enriched in certain types of proteins. Examples for these biomolecular condensates include germ P-bodies [51, 61], nucleoli [62], and stress granules [63]. These biomolecular condensates are believed to form via liquid–liquid phase separation in the cytoplasm [51, 52] and can be reconstituted in vitro [64, 65, 66, 67]. They are enriched in certain types of proteins that have intrinsically disordered domains and interact via multivalent macromolecular interactions [68, 66, 67, 69, 52].

The adhesion of condensate droplets to biomembranes and vesicles leads to different adhesion and wetting morphologies as well as to wetting transitions as we change the molecular composition or the temperature [48, 33]. Aqueous phase separation of PEG-dextran solutions within GUVs was first reported by Christine Keating and coworkers [70]. Particularly fascinating remodeling processes of membranes interacting with condensate droplets are the formation of membrane nanotubes [71, 72, 73], the formation of two spherical membrane segments that enclose two different condensate droplets [39], and the complete engulfment of the droplets by the membranes [14]. Complete engulfment of a dextran-rich condensate droplet by a GUV membrane leads to a closed membrane neck as displayed in Fig. 6d. So far, the fission of such necks has not been observed experimentally

However, neck fission and endocytosis of condensate droplets have been observed in molecular dynamics simulations, [10] in which the formation of condensate droplets was studied using the same off-lattice model for a binary water-solute mixture as in Fig. 12, but now focussing on the two-phase coexistence region of this mixture. The endocytic process starts with the spreading of the droplet onto the membrane, followed by partial or complete engulfment of the droplet. One example for partial engulfment is shown in Fig. 13, which was obtained for solute mole fraction $\Phi_S = 0.004$ and solubility $\zeta = 25/70 = 0.36$, which is located within the two-phase coexistence region of the solute-water phase diagram. Initially, both the nanodroplet and the nanovesicle are fully immersed in the liquid phase α as shown in Fig. 13a. When the droplet gets into contact with the vesicle membrane, a small contact area is formed as in Fig. 13b. After this onset of adhesion, the vesicle membrane starts to engulf the membrane. This process continues by pulling out membrane area from the thermally excited undulations, thereby increasing the bilayer tension in the membrane. Eventually, a new stable morphology, corresponding to a partially engulfed droplet, is reached as shown in Fig. 13c.

The contact line between the condensate droplet and the lipid membrane partitions this membrane into two segments, the $\alpha\gamma$ segment exposed to the aqueous bulk phase α and the $\beta\gamma$ segment in contact with the β droplet, see Fig. 13 c. The membrane area of the $\beta\gamma$ segment represents the contact area between membrane and droplet. When we now reduce the volume of the nanovesicle by osmotic deflation, the contact area further increases following three possible pathways. [10] First, a droplet of volume V cannot be completely engulfed by the vesicle membrane, if the area A of this membrane is too small and satisfies $(A/2)^3 < 36\pi V^2$ as follows from the isoperimetric inequality. On the other hand, complete engulfment is possible for $(A/2)^3 \geq 36\pi V^2$ and can then proceed in an axisymmetric or non-axisymmetric manner, depending on the line tension of the contact line between membrane and droplet.

As previously discussed in Sect. 3.9, the contact line tension λ_{co} can be positive or negative. In fact, the sign of λ_{co} is determined by the stress asymmetry between the two leaflets of the bilayer. [10] The line tension λ_{co} is negative if the bilayer is symmetric or only weakly asymmetric in the absence of the droplets and positive if the bilayer exhibits a sufficiently large stress asymmetry. [10, 33] A positive line tension leads to a circular contact line and to an axisymmetric membrane neck that becomes closed and then undergoes fission. One example for this axisymmetric process of complete engulfment and endocytosis is displayed in Fig. 14. In contrast, a negative contact line tension leads to a strongly non-circular contact line and to a tight-lipped shape of the membrane neck, which prevents the fission of this neck.

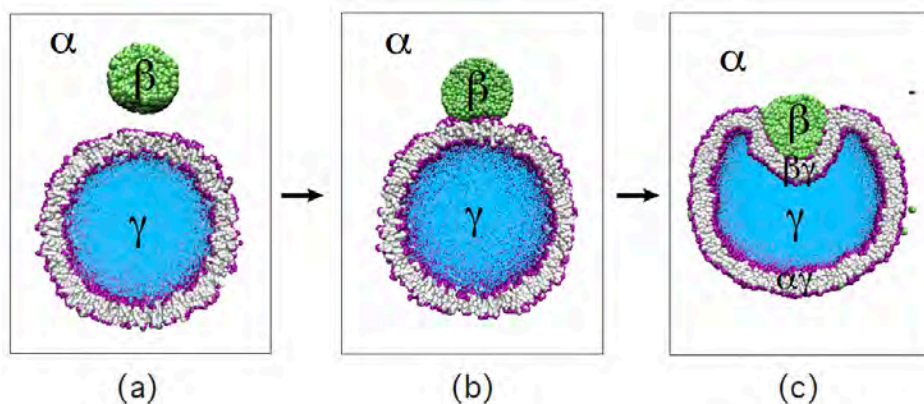


Figure 13: Partial engulfment of a condensate droplet (green) by the lipid bilayer (purple-grey) of a nanovesicle, as observed in molecular dynamics simulations. [10] The vesicle encloses the aqueous solution γ (blue). Both the nanodroplet and the nanovesicle are immersed in the aqueous bulk phase α (white): (a) Initially, the droplet is well separated from the vesicle which implies that the outer leaflet of the bilayer is only in contact with the α phase; (b) When the droplet is attracted towards the vesicle, it spreads onto the lipid bilayer, thereby forming an increasing contact area with the vesicle membrane; and (c) Partial engulfment of the droplet by the membrane after the vesicle-droplet couple has relaxed to a new stable state. The contact area between bilayer and β droplet defines the $\beta\gamma$ segment of the bilayer membrane whereas the rest of the bilayer represents the $\alpha\gamma$ segment still in contact with the α phase. Vesicle and droplet have a diameter of 37 nm and 11.2 nm, respectively.

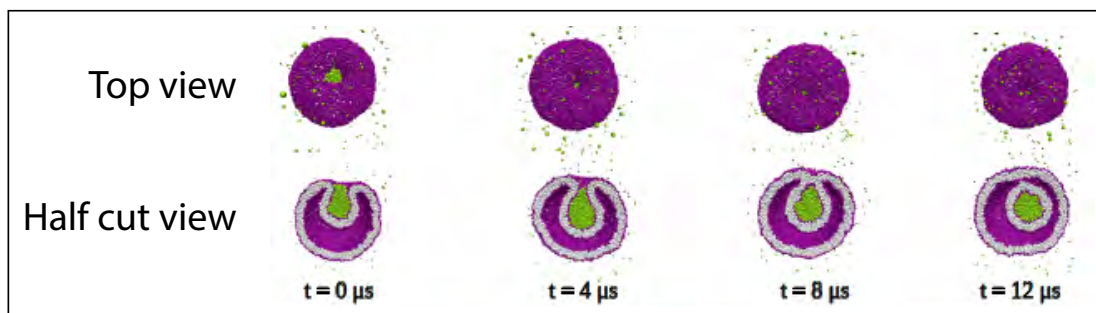


Figure 14: Endocytosis of a nanodroplet (green) *via* complete axisymmetric engulfment by the vesicle membrane (purple-grey) followed by the division of the vesicle into two nested daughter vesicles: The nanovesicle is formed by a lipid bilayer with $N_{ol} = 5500$ lipids in the outer leaflet and $N_{il} = 4600$ lipids in the inner one. The vesicle has a size of 37 nm, the droplet a diameter of 11.2 nm. The displayed time lapse starts with a reduction of the vesicle volume at time $t = 0$ which is kept constant for all later times. The membrane neck closes at $t = 4 \mu s$ and undergoes fission at $t = 9 \mu s$, generating a small intraluminal vesicle around the droplet. The latter morphology remains unchanged for at least $30 \mu s$. [10]

5 Fusion via adhesion and pore formation

We now address the process of membrane fusion, focussing again on geometric and membrane-elastic aspects. As far as the Euler characteristic χ and the topological genus \mathbf{g} are concerned, each individual fusion process represents the reverse of a fission process (Figs. 3 and 4). However, the energetics of fusion and fission is quite different. Because the fission process is exergonic or ‘downhill’ in free energy, as shown in the previous Sections 3 and 4, the fusion process must be endergonic or ‘uphill’ in free energy. In the cell, fusion processes are often coupled to the hydrolysis of ATP or GTP. From a physical point of view, the presumably simplest mechanism to drive membrane fusion is via the mechanical tension acting within one of the membranes in their prefusion state.

5.1 Membrane necks created by fusion

Let us start with the fusion of two genus-0 vesicles as depicted in panels a and c of Fig. 15. In Fig. 15a, the two vesicles enclose two mutually disjoint spatial regions and could have been formed by the fission process in Fig. 5a,b. The fusion of these mutually disjoint vesicles creates an out-budded vesicle with a narrow fusion neck as in Fig. 15b. In Fig. 15c, the larger vesicle encloses the smaller one, which could be the result of the fission process in Fig. 5c,d. The fusion of these nested vesicles creates the in-budded vesicle with a narrow membrane neck as in Fig. 15d. In the literature on membrane fusion, the membrane neck is usually denoted as the ‘fusion pore’. The term ‘fusion neck’ is used here to emphasize the intimate relation to the fission processes in Fig. 5.

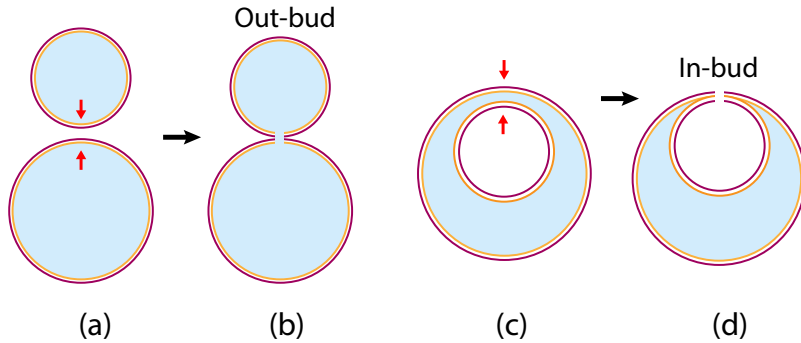


Figure 15: Formation of membrane necks via fusion starting from two genus-0 vesicles with Euler characteristic $\chi = 4$ and genus $\mathbf{g} = -1$ that fuse into a single genus-0 vesicle with $\chi = 2$ and $\mathbf{g} = 0$: (a) Two vesicles, which enclose two mutually disjoint spatial regions prior to fusion, adhere with their outer leaflets as indicated by the two red arrows; (b) Fusion then creates an out-budded genus-0 vesicle with a narrow membrane neck, reversing the two fission substeps in panels a and b of Fig. 5; (c) When the two vesicles are nested prior to fusion, the outer leaflet of the smaller one adheres to the inner leaflet of the larger one (red arrows); and (d) Fusion now creates an in-budded genus-0 vesicle with a narrow membrane neck, reversing the two fission substeps in panels c and d of Fig. 5.

5.2 Pathways of tension-induced fusion

Experimentally, tension-induced fusion was originally studied by osmotic swelling of vesicles that adhere to a planar bilayer. [74] The molecular mechanisms underlying tension-induced fusion have been visualized and elucidated by molecular dynamics simulations. [75, 76, 77] More recently, several experimental studies provided additional evidence for tension-induced fusion [78, 79, 80, 81], which can be strongly enhanced by electrostatic interactions between oppositely charged membranes [79]. In the simulations, the close proximity of two lipid bilayers can lead to a variety of alternative outcomes such as stable hemifused bilayers and bilayer rupture but fusion events were always observed within a certain range of positive bilayer tensions. Furthermore, the simulations revealed three different fusion pathways as described next.

Non-axisymmetric fusion pores after hemifusion. In our first set of simulations [76, 82], we studied the fusion of a planar bilayer with a nanovesicle, for which we observed an unusual pathway, as illustrated by the time lapse snapshots in Fig. 16. In order to visualize this pathway, the lipids in the planar bilayer have red head groups and green tails whereas the lipids in the vesicle have orange head groups and yellow tails. The observed fusion pathway proceeds via three distinct substeps. After the vesicle and the planar bilayer have come into contact at time $t = 78.5$ ns, the vesicle starts to spread onto the bilayer, thereby forming a highly curved membrane segment along the contact line with the planar bilayer. The lipids along the contact line then undergo interbilayer flips from the vesicle to the planar bilayer, see the yellow lipid tails that appear in the lower leaflet of the planar bilayer. These flips lead to the intermixing and partial fusion of the two bilayers, followed by the nucleation of a bean-shaped hemifusion diaphragm at about $t = 1177$ ns. The bean-shape of the diaphragm can be clearly seen when one looks at sections across the planar bilayer, which are perpendicular to the side view in Fig. 16. Finally, this diaphragm ruptured close to the contact line at $t = 1334$ ns, thereby opening up a strongly asymmetric fusion pore that provides a water channel between the interior vesicle solution (blue) and the water compartment (white) above the planar bilayer in Fig. 16.

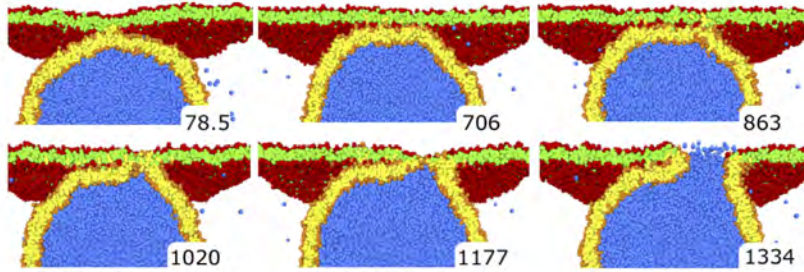


Figure 16: Fusion of a nanovesicle with a planar bilayer as observed in molecular dynamics simulations: The vesicle consists of 6869 lipids (orange heads, yellow chains) and has a diameter of 28 nm, while the planar membrane contains 6911 lipids (red heads, green chains). The nanovesicle has a diameter of 28 nm. The water beads originally inside the vesicle are blue, those outside are not shown for clarity (white background). The figure displays six time lapse snapshots which illustrate the development of the fusion process from 78.5 ns, when the first contact between the two membranes occurs and lipid tails start to undergo interbilayer flips, until the opening of the fusion pore after 1334 ns. [76]

Time scales of fusion substeps. The three substeps for the formation of an asymmetric fusion pore are governed by three tension-dependent time scales as displayed in Fig. 17, where these time scales are plotted as functions of the (projected) area per lipid, A , in the planar bilayer. This area per lipid increases with increasing bilayer tension. The time scale $\langle t_\alpha \rangle$ is the average time it takes from the initial contact between the two membranes until the first interbilayer flip. The time scale $\langle t_\beta \rangle$ is the average reordering time between the first interbilayer flip and the nucleation of the hemifused patch. The average fusion time is denoted by $\langle t_{\text{fu}} \rangle$ and the width of the fusion time distribution by Δt_{fu} .

All time scales that are plotted in Fig. 17 decay exponentially with increasing area per lipid, A , and thus with increasing bilayer tension. Such a behavior indicates that the free energy barriers that determine these time scales are reduced by the bilayer tension in a linear fashion. For tensionless bilayers, the free energy barrier is found to be about $9 k_B T$ for the interbilayer flips independent of the vesicle size, whereas the barrier for the nucleation of the hemifused diaphragm is about $12 k_B T$ for the 14-nm vesicles in Fig. 17a and about $16 k_B T$ for the 28-nm vesicles in Fig. 17b. The rupture time for the hemifused diaphragm was observed to be always between 150 and 300 ns, irrespective of the bilayer tension.

Two alternative fusion pathways. We also studied the fusion of two nanovesicles, using a somewhat different set of force parameters for the coarse-grained molecular model which made the lipid bilayers more rigid. [83, 77] As a result, we observed, depending on the magnitude of the bilayer

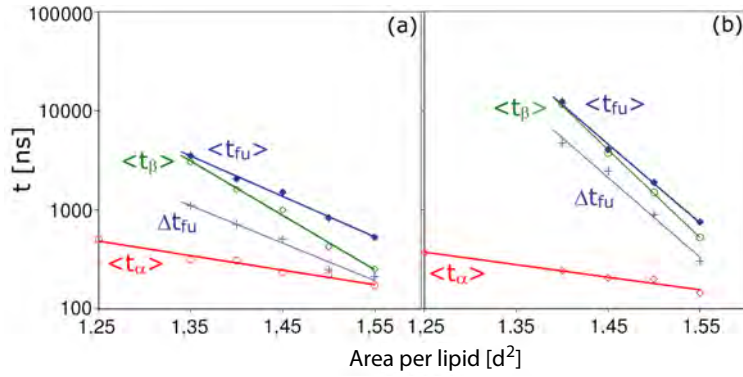


Figure 17: Different time scales for the fusion between nanovesicle and planar bilayer: The diameter of the vesicles in (a) and (b) is equal to 14 nm and 28 nm, respectively. The time scales are plotted semi-logarithmically versus the area per lipid within the planar bilayer, given in units of d^2 where d is the basic length scale of the molecular model. For the force parameters used here, the area per lipid is proportional to the bilayer tension. The different time scales are the average first flipping time $\langle t_\alpha \rangle$ (red) until the first lipid flip from the vesicle bilayer to the planar bilayer; the average reordering time $\langle t_\beta \rangle$ (green), between the first interbilayer flip and the nucleation of a hemifused patch; the average fusion time $\langle t_{fu} \rangle$ (blue); and the width Δt_{fu} of the fusion time distribution (blue). These time scales are obtained from more than 140 statistically independent simulations. A comparison of the two sets of data in (a) and (b) shows that the average first flipping time $\langle t_\alpha \rangle$ is independent of the vesicle size, whereas the average reordering time $\langle t_\beta \rangle$ increases with the size of the vesicle. [76]

tensions, two alternative fusion pathways as displayed in Figs. 18 and 19. For relatively low tensions, one of the two vesicles develops a bilayer pore within the contact area, see Fig. 18a. This pore grows in size and leads to the two-vesicle geometry as displayed in Figs. 18b. At first sight, the latter geometry resembles a hemifused state but the diaphragm between the two vesicles consists almost exclusively of lipids from the unruptured vesicle, in contrast to a hemifusion diaphragm, which would contain a mixture of lipids from the outer leaflets of both vesicles.

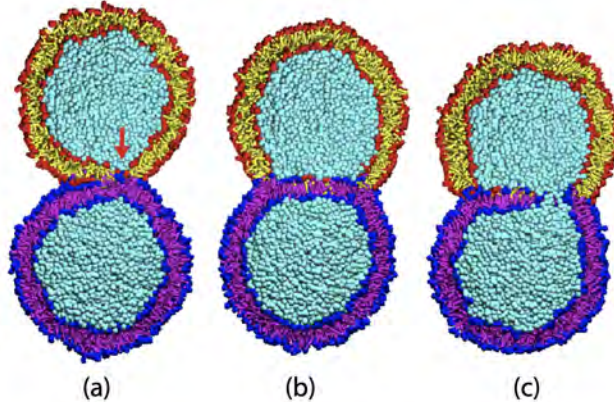


Figure 18: Low-tension pathway for two nanovesicles with more rigid bilayers: (a) The two nanovesicles adhere and form a small contact area. The lipids in the upper vesicle have red head groups and yellow tails, whereas those in the lower vesicle have blue head groups and purple tails. The adhesion generates a substantial bilayer tension, which leads to the poration of the upper bilayer close to the boundary of the contact area (red arrow). This bilayer pore grows until the upper bilayer has completely retracted from the contact area in (b). The latter geometry is different from a hemifused state because the diaphragm between the two vesicles consists almost exclusively of blue-purple lipids from the unporated vesicle bilayer. Finally, an asymmetric fusion pore is formed in (c) after the blue-purple diaphragm has ruptured. [77]

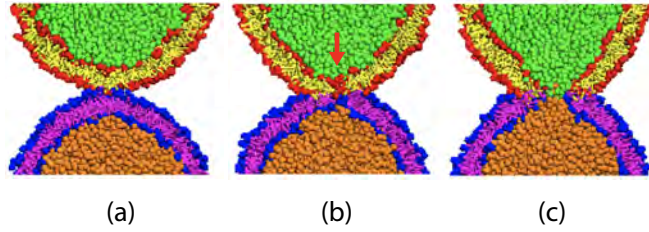


Figure 19: High-tension pathway for two nanovesicles with more rigid bilayers: (a) Local adhesive contact between the two nanovesicles; (b) Disruption of the two adhering bilayers (red arrow); and (c) Opening of a fusion pore which provides a connection between the two water compartments (orange and green) enclosed by the two vesicles. [77]

For relatively high bilayer tension, the molecular model with the stiffer lipid tails leads to the fusion pathway shown in Fig. 19. In this case, the local adhesive contact between the two vesicles leads to a relatively small contact area and to fast disruption of both bilayers. In this high-tension pathway, the fusion pore is formed without an intermediate diaphragm, see Fig. 19b.

Fusion of tensionless bilayers with stretched outer leaflets. All pathways of tension-induced fusion, discussed so far and displayed in Figs. 16 – 19, are driven by sufficiently large bilayer tensions, $\Sigma = \Sigma_{ol} + \Sigma_{il} > 0$, within the two bilayers to be fused. The positive bilayer tensions act to stretch all four leaflets of the two bilayers. However, in order to obtain vesicle fusion, it is not necessary to stretch all leaflets of the two bilayers. Indeed, it is sufficient to stretch only the two outer leaflets of the two bilayers by sufficiently large outer leaflet tensions $\Sigma_{ol} > 0$. [38] As a consequence, it is possible to obtain fusion of vesicles, which are bounded by *tensionless* bilayers with $\Sigma = \Sigma_{ol} + \Sigma_{il} = 0$, provided the outer leaflet tensions Σ_{ol} are sufficiently large and positive. One example for such a fusion event is displayed in Fig. 20.

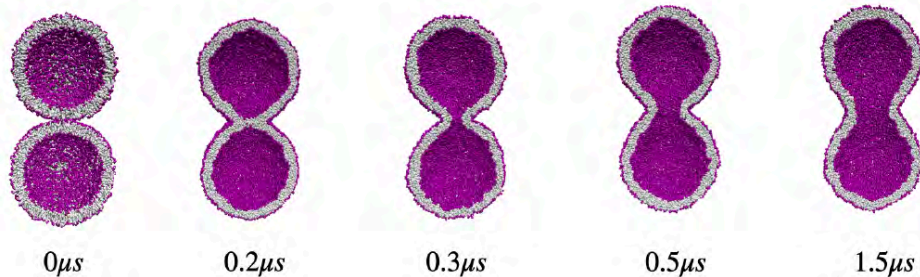


Figure 20: Time-lapse snapshots of two identical vesicles with tensionless bilayers, which fuse when their outer leaflets are stretched by a sufficiently large leaflet tension $\Sigma_{ol} > 0$. Before they come into contact, each vesicle bilayer is spherical and contains $N_{ol} = 5600$ lipids in its outer leaflet as well as $N_{il} = 4500$ lipids in its inner leaflet. The outer leaflets are stretched by the leaflet tension $\Sigma_{ol} = +1.02 k_B T/d^2$ whereas the inner leaflets are compressed by the inner leaflet tension $\Sigma_{il} = -1.02 k_B T/d^2$. Note that both vesicle bilayers are tensionless with bilayer tensions $\Sigma = \Sigma_{ol} + \Sigma_{il} = 0$. At time $t = 0 \mu s$, the two vesicles are brought into contact and promptly undergo fusion within $0.3 \mu s$. [38]

5.3 Insights from fusion simulations

First of all, our simulations revealed that even the presumably simplest driving force for fusion as provided by bilayer tension can lead to several distinct pathways. Second, these simulations demonstrated that the fusion process is stochastic in nature and that the distinct substeps are governed by different probability distributions [76, 82, 77] as illustrated by the different time scales in Fig. 16.

In hindsight, the stochastic nature of the fusion process is quite obvious because the process has to overcome one or several free energy barriers. However, the large majority of fusion simulations ignored this aspect because it is computationally quite expensive, even for coarse-grained molecular dynamics. Furthermore, our simulations revealed two more specific molecular features, interbilayer flips of splayed lipids and non-axisymmetric fusion pores.

Interbilayer flips of splayed lipids. For a splayed lipid, the two tails point in opposite directions as originally proposed in Ref. [84]. When a lipid has such a splayed conformation, it can bridge the water gap between the two adjacent bilayers in their pre-fusion state by inserting one tail into each bilayer. Some experimental evidence for this bridging conformation of splayed lipids has been obtained by fluorescence spectroscopy [85] and by using lipids with a azobenzene group that can undergo light-induced trans/cis isomerization [86]. Furthermore, splayed lipids have also been observed in other simulation studies. [87, 88, 76, 89, 90, 91, 92]

Non-axisymmetric fusion pores. To some extent, our fusion simulations were motivated by the so-called stalk model [93, 94, 95] which assumes that the fusion process proceeds via axisymmetric membrane shapes, i.e., via axisymmetric intermediates and axisymmetric fusion pores. In contrast, the simulations snapshots displayed in Figs. 16 and 18 clearly demonstrate that the fusion process can involve both strongly non-axisymmetric intermediates and non-axisymmetric fusion pores. Non-axisymmetric fusion pores have now been observed by many other groups, both in experimental and in simulation studies. [96, 97, 98, 99, 100, 101]

5.4 Mechanisms of protein-mediated fusion

Membrane fusion of cellular membranes involves the formation of protein complexes anchored to the membranes in their pre-fusion state. Three types of fusion mechanisms can be distinguished, depending on how these proteins mediate the adhesion between the membranes. The simplest fusion mechanism is observed for viral fusion proteins that are only anchored to the membrane envelope of the virus. The viral fusion protein inserts into the acceptor membrane of the host cell, a process that does not seem to require additional proteins anchored to the acceptor membrane. One example for such a viral fusion protein is provided by hemagglutinin of influenza viruses [102], another by the Spike protein of corona viruses, which contains a fusion peptide sequence within its S2 subunit [103, 104].

A second type of protein-mediated fusion mechanism is used in homotypic fusion of intracellular membrane segments that enclose the endoplasmic reticulum or belong to the outer membranes of two mitochondria. In this case, the apposing membranes are pulled together by forming trans-dimers of identical membrane proteins anchored to both membranes. These proteins have a GTPase domain that hydrolyzes GTP. Examples are proteins from the atlastin family, which drive GTP-dependent fusion of the endoplasmic reticulum membranes in multicellular animals [105, 106, 107], as well as analogous membrane GTPases such as Sey1 and RHD3, which catalyze membrane fusion in yeast [108] and plant [109] cells. Likewise, membrane GTPases from the mitofusin family drive the homotypic fusion of the outer membranes of two mitochondria. [110, 111, 112]

A third type of multiprotein complex is used along the outward secretory pathway in eukaryotic cells (red arrows in Fig. 1). This pathway, which involves the heterotypic fusion of different organelles and vesicles, is dominated by proteins from the SNARE family. [113, 114, 115] For SNARE-mediated fusion, each of the fusing membranes contributes a different set of membrane proteins to the multiprotein complex that mediates their adhesion.

6 Fusion and Fission of Multispherical Vesicles

In Figs. 5 - 7, we described $(1 + 1)$ -multispheres, which represent the simplest examples for stable multispherical shapes. In fact, the theory of curvature elasticity predicts stable multispheres consisting of an arbitrary number of (punctured) spheres connected by closed membrane necks. [7, 22] This prediction is a consequence of two general curvature-elastic features: (i) the shape equation for spherical segments is quadratic in the mean curvature of these segments; and (ii) the stability condition for

closed membrane necks as given by Eqs. (12) and (13). The quadratic nature of the shape equation implies that only up to two different sphere radii can coexist on the same vesicle. Likewise, the local nature of the stability conditions for closed membrane necks as given by Eqs. (12) and (13) ensures that these conditions can be applied to the necks of any multispherical shape.

6.1 Multispherical shapes with more than two spheres

Experimentally, a striking variety of multispherical shapes of GUVs has been observed when the GUVs were exposed to asymmetric solutions of two simple sugars, sucrose and glucose. [13, 22, 116] When the interior solution contained only sucrose and the exterior solution primarily glucose, the vesicle membranes acquired a positive spontaneous curvature of about $1/\mu\text{m}$. In general, the observed multispheres consist of N_l large spheres with radius R_l and N_s small spheres with radius R_s . In addition, special multispheres consisting of N equally sized spheres were also observed. These shapes correspond to the limiting case, in which the large-sphere-radius R_l and the small-sphere-radius R_s become equal, transforming the $(N_l + N_s)$ -multisphere into an N -multisphere with $N = N_l + N_s$. Several examples of N -multispheres are displayed in Fig. 21.

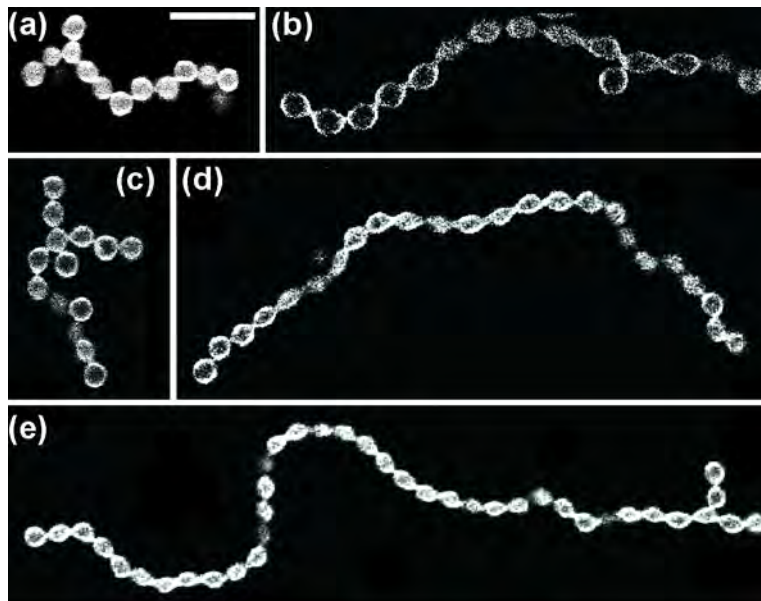


Figure 21: Multispherical shapes of giant unilamellar vesicles with positive spontaneous curvature, consisting of with N equally sized spheres as observed by light microscopy . [13] The sphere number N is equal to $N = 14$ in (a), $N = 15$ in (b) and (c), $N = 24$ in (d), and $N = 39$ in (e). All (N_*) -multispheres provide examples for constant-mean-curvature surfaces. Furthermore, apart from (d), all N -multispheres displayed here exhibit multispherical junctions. Each junction consists of one central sphere that is connected to more than two neighboring spheres. Scale bar in (a) is $10 \mu\text{m}$ and applies to all panels. In spite of their complex morphology, all multispherical shapes displayed in this figure have the same genus-0 topology as a single sphere.

It is interesting to note that the N -multispheres represent constant-mean-curvature (CMC) surfaces. [22] For a long time, the only examples for freely suspended CMC surfaces with nonzero mean curvature were provided by the unduloids of Delaunay [117], which provide a one-parameter family of tubular shapes that interpolate smoothly between multispherical tubes consisting of equally sized (and punctured) spheres and cylindrical tubes. More recently, additional CMC surfaces have been constructed by perturbing a cluster of identical spheres that touch each other. [118, 119, 120, 121, 122] One example are triunduloids [121, 122] that consist of three unduloidal arms connected by a central core. These triunduloids provide smoothly curved shapes with a low bending energy for the three-way junctions observed in the endoplasmic reticulum, see Fig. 2a. [123]

In the research field of CMC surfaces, the physical system used to motivate these surfaces are the

shapes of soap films and liquid droplets. However, when the initial cluster of identical and touching spheres is viewed as a cluster of liquid droplets, the resulting CMC surface is not stable. Indeed, the cluster will either fall apart and then form many small droplets or it will coalesce into one large droplet that will eventually attain the shape of a single sphere. In contrast, when the initial cluster of droplets is enclosed by a membrane, this membrane can lead to a stable multispherical shape as predicted theoretically [7] and observed experimentally [13], see examples in Fig. 21.

6.2 Formation of higher genus vesicles by fusion

The multispherical shapes in Fig. 21 consist of spheres with a radius of the order of $1\ \mu\text{m}$. This size is convenient in order to observe the multispherical shapes by conventional light microscopy. One can reduce the size of the spherical vesicles to a diameter below 100 nm by the preparation of liposomes and proteoliposomes. Furthermore, proteoliposomes that contain a membrane GTPase such as atlastin, fuse with each other and form long nanotubular structures after the addition of GTP. [105, 106, 124, 125] The diameter of these nanotubes has been estimated by electron microscopy to be below 50 nm [124].

Homotypic fusion of proteoliposomes. To obtain some insight into the formation of nanotubes from proteoliposomes, we will now consider N proteoliposomes that undergo homotypic fusion to form an N -multisphere. In the absence of GTP, the proteoliposomes are taken to be relaxed in the sense that the mean curvature of their membrane is close to the membrane's spontaneous curvature m , which implies that the radius R of the proteoliposomes is close to $1/m$ and that their bending energy in Eq. (5) is close to zero. The dimensionless shape parameters v and \bar{m} , as defined in Eqs. (9) and (10), are then equal to $v = v_1 = 1$ and $\bar{m} = \bar{m}_1 = 1$ for each proteoliposome. When we add GTP, the proteoliposomes start to fuse to form multispherical shapes. More precisely, the fusion of N proteoliposomes leads to a multisphere with the shape parameters $v = v_N \equiv 1/\sqrt{N}$ and $\bar{m} = \bar{m}_N \equiv \sqrt{N}$, provided both the total membrane area and the total vesicle volume are conserved during the fusion process. For $N = 2$, the shape parameters $v = v_2$ and $\bar{m} = \bar{m}_2$ correspond to the corner point of the stability regime in Fig. 7b, at which the two lines of limit shapes, L_{1+1} and L_{2*} , meet. For $N > 2$, the shape parameters $v = v_N$ and $\bar{m} = \bar{m}_N$ define analogous corner points of the corresponding stability regimes. [22]

The nanotube shapes can be resolved by super-resolution microscopy, which has not been reported, so far, for the nanotubes reconstituted from proteoliposomes. However, structured illumination microscopy has been applied to reticular nanotubes *in vivo*, [126, 2] which revealed that these shapes resemble unduloids. In the (\bar{m}, v) morphology diagram, unduloids with minimal bending energy are found for $\bar{m} < \bar{m}_N$ and for $v < v_N$. Such unduloid shapes will form *via* the fusion of proteoliposomes when some membrane proteins get lost during the fusion process, thereby reducing the spontaneous curvature \bar{m} , or if the fusion process is leaky and the interior volume of the proteoliposomes is not conserved during the process.

Homotypic fusion of multispherical tubes. Now, let us assume that we have obtained a multispherical tube consisting of N equally sized spheres. One example with $N = 18$ is displayed in Fig. 22. The tubular membrane contains membrane proteins that can hydrolyse GTP, thereby driving homotypic fusion between different membrane segments. In Fig. 22a, we start from an unbranched multispherical tube with topological genus $\mathbf{g} = 0$ in the absence of GTP. When we add GTP, the two terminal spheres can fuse, which leads to a multispherical tube with $\mathbf{g} = 1$ and no junctions as shown in Fig. 22b. In fact, one of the terminal spheres may fuse with any other sphere of the multispherical tube, again producing a multisphere with $\mathbf{g} = 1$, which now involves a three-way junction. A somewhat more complex shape evolution is depicted in Fig. 22c-e. We now start, in the absence of GTP, with a genus-0 multisphere that consists of a four-way junction with four linear tube segments. After the addition of GTP, homotypic fusion of the two terminal spheres below the junction now leads to the genus-1 multisphere in Fig. 22d. One additional fusion event between the two terminal spheres above the junction then leads to the genus-2 multisphere in Fig. 22e.

Adding more multispherical tubes to the small networks displayed in Fig. 22 as well as GTP, the homotypic fusion between different membrane segments will create tubular networks with a large

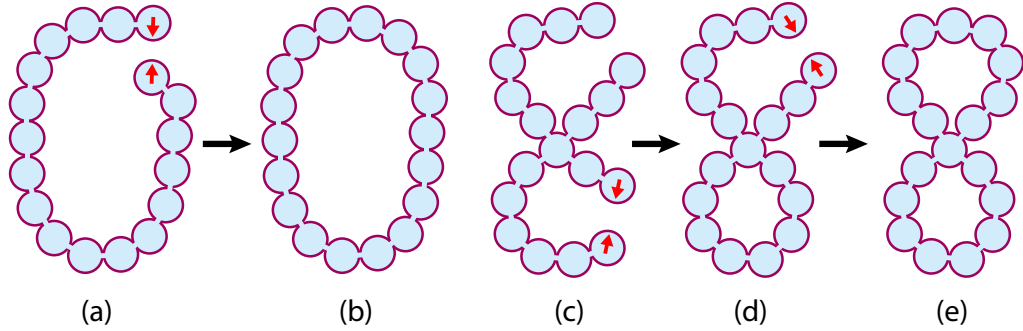


Figure 22: Self-adhesion and fusion of multispherical tubes with $N = 18$ equally sized spheres: (a) Genus-0 multisphere with 18 spheres connected by 17 membrane necks. Fusion of the two terminal ends (red arrows) creates the genus-1 multisphere in (b) with 18 spheres and 18 necks; (c) Genus-0 multisphere with 18 spheres, 17 necks, and one four-way junction, which is formed by the sphere with four membrane necks. Fusion of the two terminal spheres in the lower toroidal ring (red arrows) leads to the genus-1 shape in (d) with 18 spheres and 18 necks; and (d) Fusion of the two terminal spheres in the upper toroidal ring (red arrows) creates the genus-2 shape in (e) with 18 spheres and 19 necks.

genus, which resemble the ER networks in Fig. 2. However, these networks can exhibit junctions with more than three necks. One example is the network in Fig. 22c, which involves a four-way junction, consisting of a central sphere that is connected to four neighboring spheres *via* four membrane necks. It has been argued elsewhere that the predominance of three-way junctions in the ER arises from a significant bilayer tension that acts to stretch the membrane nanotubes. [22, 123]

6.3 Fission of higher genus vesicles

Finally, we will illustrate the fission of higher genus vesicles by looking at the cleavage of the multispherical tubes in panels b and e of Fig. 22. These membrane tubes exhibit many membrane necks, each of which is governed by the stability relation in Eq. (12) and compressed by the constriction force in Eq. (17). Thus, in order to cleave one of these necks, we may simply increase the spontaneous curvature m , e.g., by binding His-tagged GFP to the outer leaflets of the tube membranes, a procedure that was successfully used for the genus-0 dumbbell vesicles in Figs. 8 and 10. After one of the necks in Fig. 22 has been cleaved, we obtain the multispherical shapes in Fig. 23.

For a laterally uniform membrane, each neck is subject to the same constriction force which implies that the fission time is governed by the same dwell time distribution. This degeneracy is lifted if the neck contains a domain boundary, separating two distinct intramembrane domains, because the line tension λ_{db} of the domain boundary enhances the constriction force as described by Eq. (21). Likewise, if one of the spheres engulfs an adhesive particle or condensate droplet, the necks connected to this sphere will experience the enhanced constriction force described by Eq.(24).

7 Summary and Outlook

In this review, recent insights about the topological transformations of biomembranes and vesicles have been described in order to further elucidate the physical mechanisms for these processes. These transformations can be characterized in a very general manner by changes in the Euler characteristic χ and in the topological genus g (Figs. 3 and 4). We then addressed fission processes which are controlled by constriction forces that compress closed membrane necks. For laterally uniform membranes, these forces are described by Eqs. (17) and (18) for the necks of out- and in-buds, respectively. The constriction forces are enhanced by the line tension λ_{db} of a domain boundary, residing in the neck, see Eqs. (21) and (22), as well as by adhesive particles or droplets engulfed by the membranes, see Eqs. (24) and (26). A sufficiently large constriction force leads to the fission of the membrane neck as observed for the division of GUVs (Figs. 8 and 10), for the division of nanovesicles (Figs. 11 and

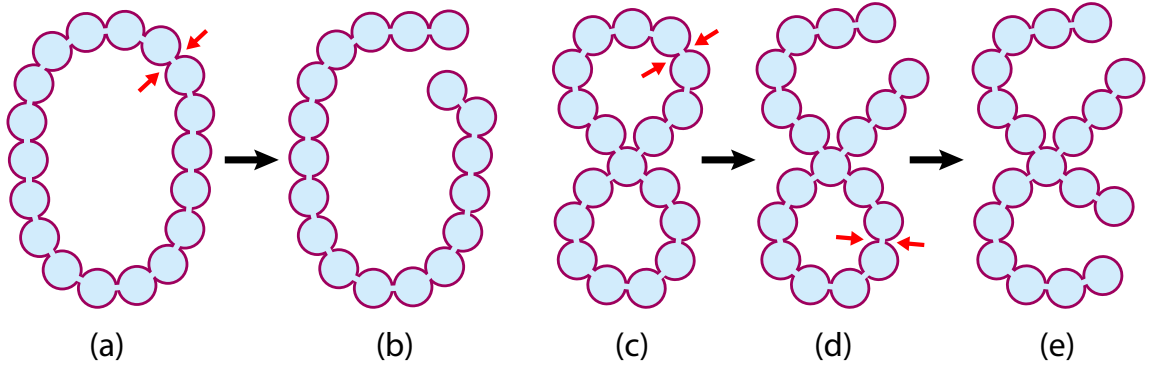


Figure 23: Fission of genus-1 and genus-2 vesicles, illustrated for multispheres consisting of $N = 18$ equally sized spheres: (a) Genus-1 multisphere with 18 spheres connected by 18 membrane necks. Cleavage of one neck (red arrows) leads to the genus-0 multisphere in (b) with 18 spheres and 17 necks. This fission process reverses the fusion process in panels a and b of Fig 22; (c) Genus-2 multisphere with 18 spheres connected by 19 membrane necks. Cleavage of one neck in the upper toroidal ring (red arrows) leads to the genus-1 multisphere in (d) with 18 spheres and 18 necks; and (d) Another neck cleavage in the lower toroidal ring (red arrows) leads to the genus-0 multisphere in (e) with 18 spheres and 17 necks.

12b), and for the endocytosis of condensate droplets by nanovesicles (Fig. 14).

Topological transformations by fusion were discussed in Section 5. On the one hand, it was emphasized that the fusion process involves the same membrane shapes as fission, but in reversed order, as one concludes from a comparison of Fig. 15 with Fig 5. On the other hand, the ‘local surgery’ of the adhering bilayers can proceed via different intermediates, as illustrated by Figs. 16 – 20 for tension-induced fusion, which represents the simplest driving force for membrane fusion. Likewise, protein-mediated fusion processes can involve different intermediate conformations of the proteins as briefly discussed in Section 5.4, where we distinguish viral fusion from homotypic and heterotypic fusion.

The final Section 6 was devoted to multispherical vesicles, as predicted by the theory of curvature elasticity [7, 22] and experimentally observed for GUVs exposed to aqueous solutions of simple sugars [13, 116]. We focussed on multispherical tubes consisting of N equally sized spheres as displayed in Figs. 21 - 23. So far, all experimentally observed multispheres were genus-0 vesicles and had the same topology as a single sphere (Fig. 21). We then performed a ‘Gedankenexperiment’ by doping the vesicle membranes in Fig. 21 with membrane proteins that are capable of homotypic fusion in the presence of GTP. These fusion processes were illustrated by some simple examples in Fig. 22, corresponding to the formation of genus-1 and genus-2 multispheres. The fission of these vesicles as displayed in Fig. 23 can be accomplished by binding His-tagged GFP to the outer leaflets of the multispherical membranes, a method that was previously used for the division of (1+1)-vesicles (Figs. 8 and 10).

In the context of synthetic biology, one long-term challenge is to mimick the vesicular traffic in eukaryotic cells as schematically shown in Fig. 1. The vesicles are generated by the formation of buds from donor membranes and by the fission of the resulting membrane necks (Fig. 4a). These vesicles move across the cell and are eventually reintegrated into different membrane-bound organelles by adhesion to the acceptor membranes of these organelles and by the subsequent fusion between vesicle and acceptor membrane (Fig. 4b). In a steady state, the two processes balance each other and lead to an average membrane area that is approximately constant. Such a balance should hold on time scales that are small compared to the mean lifespan (or turnover time) of the cells. The latter time scale depends on the cell type and varies over many orders of magnitude but the mean lifespan of human cells always exceeds a couple of days. [127].

In order to obtain a steady state between fission and fusion processes, one can start from GUVs exposed to condensate droplets in the exterior solution. A reduction of the GUV volume *via* osmotic deflation will lead to the endocytic uptake of the droplets by the GUVs, thereby generating intralu-

minal vesicles as in Fig. 14. The fusion of these intraluminal vesicles with the GUV membrane can be triggered by adding caged GTP [128] to the interior solution of the GUV and by doping the GUV membranes with atlastin or another membrane-bound GTPase for homotypic fusion (Section 5.4). When the GTP is uncaged by exposure to light and hydrolyzed by the membrane-bound atlastin, the intraluminal vesicles will fuse with the GUV membrane, thereby releasing the condensate droplets back to the exterior solution. The latter process will be facilitated by increasing the bilayer tension within the GUV membrane via osmotic inflation, which also leads to an increase in the GUV volume. One can then start another cycle of fission and fusion by osmotic deflation and inflation where the GTP remains caged during deflation but becomes uncaged during inflation.

Abbreviations

ATP: Adenosine triphosphate
CMC: constant-mean-curvature
ER: Endoplasmic reticulum
GFP: Green fluorescent protein
GTP: Guanosine triphosphate
GTPase: Enzyme that hydrolyzes GTP
GUV: Giant unilamellar vesicle
His-tag: Histidine-tag
PEG: Polyethylene glycol

Acknowledgements

I thank Rikhia Ghosh for her exploratory vesicle simulations, which led to the time lapse snapshots in Figs. 11 and 20, as well as all my collaborators for enjoyable interactions. This paper is dedicated to the memory of Michael E. Fisher, with whom I had very stimulating and fruitful interactions for many years, in particular from 1984 until 1986, when I was a postdoc in his group at Cornell University. We published several joint papers on wetting phenomena. Such phenomena have now reemerged as important aspects of condensate droplets in living cells.

References

- [1] B. Alberts, D. Bray, A. Johnson, J. Lewis, M. Raff, K. Roberts, and P. Walter. *Essential cell biology: An introduction to the molecular biology of the cell*. Garland, New York, 1998.
- [2] C. J. Obara, A. S. Moore, and J. Lippincott-Schwartz. Structural Diversity within the Endoplasmic Reticulum - From the Microscale to the Nanoscale. *Cold Spring Harb. Perspect. Biol.*, doi: 10.1101/cshperspect.a041259, 2022.
- [3] M. Terasaki, L. B. Chen, and K. Fujiwara. Microtubules and the Endoplasmic Reticulum Are Highly Interdependent Structures. *J. Cell. Biol.*, 103:1557–1568, 1986.
- [4] C. Lee and L. B. Chen. Dynamic Behavior of Endoplasmic Reticulum in Living Cells. *Cell*, 54:37–46, 1988.
- [5] O. Baumann and B. Walz. Endoplasmic Reticulum of Animal Cells and Its Organization into Structural and Functional Domains. *Int. Rev. Cyt.*, 205, 2001.

- [6] M.P. do Carmo. *Differential geometry of curves and surfaces*. Prentice-Hall, Englewood Cliffs, NJ, USA, 1976.
- [7] R. Lipowsky. *Understanding and controlling the morphological complexity of biomembranes*, volume 30 of *Advances in Biomembranes and Lipid Self-Assembly*, chapter 3, pages 105–155. Elsevier, London, UK, 2019.
- [8] J. Steinkühler, R. L. Knorr, Z. Zhao, T. Bhatia, S. Bartelt, S. Wegner, R. Dimova, and R. Lipowsky. Controlled division of cell-sized vesicles by low densities of membrane-bound proteins. *Nature Commun.*, 11:905, 2020.
- [9] R. Ghosh, V. Satarifard, A. Grafmüller, and R. Lipowsky. Budding and Fission of Nanovesicles induced by membrane adsorption of small solutes. *ACS Nano*, 15:7237–7248, 2021.
- [10] R. Ghosh, V. Satarifard, and R. Lipowsky. Different pathways for engulfment and endocytosis of droplets by nanovesicles. *Nature Commun.*, 14:615, 2023.
- [11] R. Lipowsky. Remodeling of Membrane Shape and Topology by Curvature Elasticity and Membrane Tension. *Adv. Biology*, 6:2101020, 2022.
- [12] R. Ghosh, V. Satarifard, A. Grafmüller, and R. Lipowsky. Spherical Nanovesicles Transform into a Multitude of Nonspherical Shapes. *Nano Lett.*, 19:7703–7711, 2019.
- [13] T. Bhatia, S. Christ, J. Steinkühler, R. Dimova, and R. Lipowsky. Simple sugars shape giant vesicles into multispheres with many membrane necks. *Soft Matter*, 16:1246–1258, 2020.
- [14] Yanhong Li, H. Kusumaatmaja, R. Lipowsky, and R. Dimova. Wetting-induced budding of vesicles in contact with several aqueous phases. *J. Phys. Chem. B*, 116:1819–1823, 2012.
- [15] W. Helfrich. Elastic properties of lipid bilayers: Theory and possible experiments. *Z. Naturforsch.*, 28c:693–703, 1973.
- [16] U. Seifert, K. Berndl, and R. Lipowsky. Shape transformations of vesicles: phase diagram for spontaneous curvature and bilayer coupling model. *Phys. Rev. A*, 44:1182–1202, 1991.
- [17] R. Lipowsky. Understanding giant vesicles: A theoretical perspective. In R. Dimova and C. Marques, editors, *The Giant Vesicle Book*, chapter 5, pages 73–168. Taylor & Francis, 2020.
- [18] H.J. Deuling and W. Helfrich. The curvature elasticity of fluid membranes: A catalogue of vesicle shapes. *J. Physique*, 37:1335–1345, 1976.
- [19] U. Seifert, L. Miao, H.-G. Döbereiner, and M. Wortis. Budding transition for bilayer fluid vesicles. In R. Lipowsky, D. Richter, and K. Kremer, editors, *The Structure and Conformation of Amphiphilic Membranes*, Springer Proceedings in Physics, pages 93–96. Springer-Verlag, 1992.
- [20] H.-G. Döbereiner, E. Evans, M. Kraus, U. Seifert, and M. Wortis. Mapping vesicle shapes into the phase diagram: A comparison of experiment and theory. *Phys. Rev. E*, 55(4):4458 – 4474, 1997.

- [21] S. Svetina and B. Žekš. Shape Behavior of Lipid Vesicles as the Basis of Some Cellular Processes. *The Anatomical Record*, 268:215–225, 2002.
- [22] R. Lipowsky. Multispherical shapes of vesicles highlight the curvature elasticity of biomembranes. *Adv. Colloid Interface Sci.*, 301:102613, 2022.
- [23] B. Fourcade, L. Miao, M. Rao, M. Wortis, and R.K.P. Zia. Scaling analysis of narrow necks in curvature models of fluid lipid–bilayer vesicles. *Phys. Rev. E*, 49:5276–5286, 1994.
- [24] F. Jülicher and R. Lipowsky. Domain-induced budding of vesicles. *Phys. Rev. Lett.*, 70:2964–2967, 1993.
- [25] P. Yang, Q. Du, and Z. C. Tu. General neck condition for the limit shape of budding vesicles. *Phys. Rev. E*, 95:042403, 2017.
- [26] S. Christ, T. Litschel, P. Schwille, and R. Lipowsky. Active shape oscillations of giant vesicles with cyclic closure and opening of membrane necks. *Soft Matter*, 17:319–330, 2021.
- [27] A. Roux, G. Koster, M. Lenz, B. Sorre, J.-B. Manneville, P. Nassoy, and P. Bassereau. Membrane curvature controls dynamin polymerization. *PNAS*, 107(9):4242 – 4146, 2010.
- [28] J. Schoeneberg, M. R. Pavlin, S. Yan, M. Righini, I.-H. Lee, L.-A. Carlson, A. H. Bahrami, D. H. Goldman, X. Ren, G. Hummer, C. Bustamante, and J. H. Hurley. ATP-dependent force generation and membrane scission by ESCRT-III and Vps4. *Science*, 362:1423 – 1428, 2018.
- [29] J. Xiao and E. D. Goley. Redefining the roles of the FtsZ-ring in bacterial cytokinesis. *Curr. Opin. Microbiol.*, 34:90 – 96, 2016.
- [30] U. Seifert and R. Lipowsky. Adhesion of vesicles. *Phys. Rev. A*, 42:4768–4771, 1990.
- [31] J. Agudo-Canalejo and R. Lipowsky. Critical Particle Sizes for the Engulfment of Nanoparticles by Membranes and Vesicles with Bilayer Asymmetry. *ACS Nano*, 9:3704–3720, 2015.
- [32] J. Agudo-Canalejo and R. Lipowsky. Stabilization of membrane necks by adhesive particles, substrate surfaces, and constriction forces. *Soft Matter*, 12:8155–8166, 2016.
- [33] R. Lipowsky. Remodeling of Biomembranes and Vesicles by Adhesion of Condensate Droplets. *Membranes*, 13:223, 2023.
- [34] A. Derzhanski, A. G. Petrov, and M. D. Mitov. Molecular Asymmetry and Saddle-Splay Elasticity in Lipid Bilayers. *Ann. Phys.*, 3:297, 1978.
- [35] S. Lorenzen, R.-M. Servuss, and W. Helfrich. Elastic Torques about Membrane Edges: A Study of Pierced Egg Lecithin Vesicles. *Biophys. J.*, 50:565–572, 1986.
- [36] Mingyang Hu, J. J. Briguglio, and M. Deserno. Determining the Gaussian Curvature Modulus of Lipid Membranes in Simulations. *Biophys. J.*, 102(6):1403–1410, 2012.

- [37] V. Satarifard, A. Grafmüller, and R. Lipowsky. Nanodroplets at Membranes Create Tight-Lipped Membrane Necks via Negative Line Tension. *ACS Nano*, 12:12424–12435, 2018.
- [38] R. Lipowsky, R. Ghosh, V. Satarifard, A. Sreekumari, M. Zamaletdinov, B. Różycki, M. Miettinen, and A. Grafmüller. Leaflet tensions control the spatio-temporal remodeling of lipid bilayers and nanovesicles. *Biomolecules*, 13:926, 2023.
- [39] M. Andes-Koback and C. D. Keating. Complete budding and asymmetric division of primitive model cells to produce daughter vesicles with different interior and membrane compositions. *JACS*, 133(24):9545–9555, 2011.
- [40] M. Osawa and H. P. Erickson. Liposome division by a simple bacterial division machinery. *PNAS*, 110(27):11000 – 1004, 2013.
- [41] W. T. Snead, C. C. Hayden, A. K. Gadok, C. Zhao, E. M. Lafer, P. Rangamani, and J. C. Stachowiak. Membrane fission by protein crowding. *Proc. Nat. Acad. Sci. USA*, 114:E3258–E3267, 2017.
- [42] S. Deshpande, W. K. Spoelstra, M. van Doorn J. Kerssemakers, and C. Dekker. Mechanical Division of Cell-Sized Liposomes. *ACS Nano*, 12:2560–2568, 2018.
- [43] T. Litschel, B. Ramm, R. Maas, M. Heymann, and P. Schwille. Beating Vesicles: Encapsulated Protein Oscillations Cause Dynamic Membrane Deformations. *Angew. Chemie Int. Ed.*, 57:16286–16290, 2018.
- [44] Y. Dreher, K. Jahnke, E. Bobkova, J. P. Spatz, and K. Göpfrich. Division and regrowth of phase-separated giant unilamellar vesicles. *Angew. Chemie Int. Ed.*, 60:10661–10669, 2021.
- [45] Z. Hu, E. P. Gogol, and J. Lutkenhaus. Dynamic assembly of MinD on phospholipid vesicles regulated by ATP and MinE. *Proc. Natl. Acad. Sci.*, 99:6761–6766, 2002.
- [46] A. Sreekumari and R. Lipowsky. Large stress asymmetries of lipid bilayers and nanovesicles generate lipid flip-flops and bilayer instabilities. *Soft Matter*, 18:6066–6078, 2022.
- [47] P. A. Albertsson. *Partition of Cell Particles and Macromolecules: Separation and Purification of Biomolecules, Cell Organelles Membranes, and Cells in Aqueous Polymer Two-Phase Systems and Their Use in Biochemical Analysis and Biotechnology*. Wiley, 3 edition, 1986.
- [48] Yanhong Li, R. Lipowsky, and R. Dimova. Transition from complete to partial wetting within membrane compartments. *JACS*, 130:12252 – 12253, 2008.
- [49] R. Dimova and R. Lipowsky. Giant Vesicles Exposed to Aqueous Two-Phase Systems: Membrane Wetting, Budding Processes, and Spontaneous Tubulation. *Adv. Mater. Interf.*, 4:1600451, 2017.
- [50] J. Esquena. Water-in-water (W/W) emulsions. *Curr. Opin. Colloid Interface Sci.*, 25:109–119, 2016.

- [51] C. P. Brangwynne, C. R. Eckmann, D. S. Courson, A. Rybarska, C. Hoege, J. Gharakhani, F. Jülicher, and A. A. Hyman. Germline P Granules Are Liquid Droplets That Localize by Controlled Dissolution/Condensation. *Science*, 324:1729 – 1732, 2009.
- [52] S. F. Banani, H. O. Lee, A. A. Hyman, and M. K. Rosen. Biomolecular condensates: organizers of cellular biochemistry. *Nature Rev.: Mol. Cell Biol.*, 18:285–295, 2017.
- [53] R. Fesce, F. Grohovaz, F. Valtorta, and J. Meldolesi. Neurotransmitter Release: Fusion or ‘Kiss-and-run’? *Trends in Cell Biology*, 4(1-4), 1994.
- [54] R. G. W Staal, E. V. Mosharov, and D. Sulzer. Dopamine Neurons Release Transmitter via a Flickering Fusion Pore. *Nature Neuroscience*, 7:341–346, 2004.
- [55] R. M. Wightman and C. L. Haynes. Synaptic Vesicles Really Do Kiss and Run. *Nature Neuroscience*, 7:321–322, 2004.
- [56] H. Noguchi and M. Takasu. Adhesion of Nanoparticles to Vesicles: a Brownian Dynamics Simulation. *Biophys. J.*, 83:299–308, 2002.
- [57] A. J. Markvoort, P. Spijker, A. F. Smeijers, K. Pieterse, R. A. van Santen, and P. A. J. Hilbers. Vesicle Deformation by Draining: Geometrical and Topological Shape Changes. *J. Phys. Chem. B*, 113:8731–8737, 2009.
- [58] N. Urakami, T. Jimbo, Y. Sakuma, and M. Imai. Molecular Mechanism of Vesicle Division Induced by Coupling Between Lipid Geometry and Membrane Curvatures. *Soft Matter*, 14:3018–3027, 2018.
- [59] X. Li, Y. Liu, L. Wang, M. Deng, and H. Liang. Fusion and Fission Pathways of Vesicles From Amphiphilic Triblock Copolymers: a Dissipative Particle Dynamics Simulation Study. *Phys. Chem. Chem. Phys.*, 11:4051–4059, 2009.
- [60] M. Pannuzzo, Z. A. McDargh, and M. Deserno. The Role of Scaffold Reshaping and Disassembly in Dynamin Driven Membrane Fission. *eLife*, 7:e39441, 2018.
- [61] A. W. Fritsch, A. F. Diaz-Delgadillo, O. Adame-Arana, C. Hoege, M. Mittasch, M. Kreysing, M. Leaver, A. A. Hyman, F. Jülicher, and C. A. Weber. Local thermodynamics govern formation and dissolution of *Caenorhabditis elegans* P granule condensates. *PNAS*, 118(37):e2102772118, 2021.
- [62] J. Berry, S. C. Weber, N. Vaidya, M. Haatajaa, and C. P. Brangwynne. RNA transcription modulates phase transition-driven nuclear body assembly. *Proc. Natl. Acad. Sci. USA*, 112:E5237–E5245, 2015.
- [63] S. Jain, J. R. Wheeler, R. W. Walters, A. Agrawal, A. Barsic, and R. Parker. ATPase-Modulated Stress Granules Contain a Diverse Proteome and Substructure. *Cell*, 164:487 – 498, 2016.
- [64] P. Li, S. Banjade, H.-C. Cheng, S. Kim, B. Chen, L. Guo, M. Llaguno, J. V. Hollingsworth, D. S. King, S. F. Banani, P. S. Russo, Q.-X. Jiang, B. T. Nixon, and M. K. Rosen. Phase transitions in the assembly of multivalent signalling proteins. *Nature*, 483:336 – 341, 2012.

- [65] A. Patel, H. O. Lee, L. Jawerth, S. Maharana, M. Jahnel, M. Y. Hein, S. Stoykov, J. Mahamid, S.Saha, T. M. Franzmann, S. Grill, D. Drechsel, A. A. Hyman, and S. Alberti. A Liquid-to-Solid Phase Transition of the ALS Protein FUS Accelerated by Disease Mutation. *Cell*, 162:1066 – 1077, 2015.
- [66] Y. Lin, D. S. W. Protter, M. K. Rosen, and R. Parker. Formation and Maturation of Phase-Separated Liquid Droplets by RNA-Binding Proteins. *Mol. Cell*, 60:208 – 219, 2015.
- [67] A. Molliex, J. Temirov, J. Lee, H. J. Kim, T. Mittag, and J. P. Taylor. Phase Separation by Low Complexity Domains Promotes Stress Granule Assembly and Drives Pathological Fibrillization. *Cell*, 163:123 – 133, 2015.
- [68] T. W. Han, M. Kato, S. Xie, L. C. Wu, H. Mirzaei, J. Pei, M. Chen, Y. Xie, J. Allen, G. Xiao, and S. L. McKnight. Cell-free Formation of RNA Granules: Bound RNAs Identify Features and Components of Cellular Assemblies. *Cell*, 149:768 – 779, 2012.
- [69] L. Guo and J. Shorter. It’s Raining Liquids: RNA Tunes Viscoelasticity and Dynamics of Membraneless Organelles. *Mol. Cell*, 60:189 – 192, 2015.
- [70] M.R. Helfrich, L.K. Mangeney-Slavin, M.S. Long, K.Y. Djoko, and C.D. Keating. Aqueous Phase Separation in Giant Vesicles. *J. Am. Chem. Soc. (JACS)*, 124:13374–13375, 2002.
- [71] Yanhong Li, R. Lipowsky, and R. Dimova. Membrane nanotubes induced by aqueous phase separation and stabilized by spontaneous curvature. *Proc. Nat. Acad. Sci. USA*, 108:4731–4736, 2011.
- [72] R. Lipowsky. Spontaneous tubulation of membranes and vesicles reveals membrane tension generated by spontaneous curvature. *Faraday Discuss.*, 161:305–331, 2013.
- [73] Yonggang Liu, J. Agudo-Canalejo, A. Grafmüller, R. Dimova, and R. Lipowsky. Patterns of flexible nanotubes formed by liquid-ordered and liquid-disordered membranes. *ACS Nano*, 10:463–474, 2016.
- [74] J. Zimmerberg A. Finkelstein and F.S. Cohen. Osmotic swelling of vesicles: its role in the fusion of vesicles with planar phospholipid bilayer membranes and its possible role in exocytosis. *Anu. Rev. Physiol.*, 48:163–174, 1986.
- [75] J. Shillcock and R. Lipowsky. Tension-induced fusion of bilayer membranes and vesicles. *Nature Materials*, 4:225–228, 2005.
- [76] A. Grafmüller, J. Shillcock, and R. Lipowsky. Pathway of Membrane Fusion with Two Tension-Dependent Energy Barriers. *Phys. Rev. Lett.*, 98:218101, 2007.
- [77] Lianghai Gao, R. Lipowsky, and J. C. Shillcock. Tension-induced vesicle fusion: pathways and pore dynamics. *Soft Matter*, 4:1208–1214, 2008.
- [78] T.-T.Kliesch, J. Dietz, L. Turco, P. Halder, E. Polo, Marco Tarantola, R. Jahn, and A. Janshoff. Membrane tension increases fusion efficiency of model membranes in the presence of SNAREs. *Sci. Rep.*, 7:12070, 2017.

- [79] R. B. Lira, T. Robinson, R. Dimova, and K. A. Riske. Highly Efficient Protein-free Membrane Fusion: A Giant Vesicle Study. *Biophys. J.*, 116:79 – 91, 2019.
- [80] I. Ivanov, R. B. Lira, T.-Y. D. Tang, T. Franzmann, A. Klosin, L. C. da Silva, A. A. Hyman, K. Landfester, R. Lipowsky, K. Sundmacher, and R. Dimova. Directed Growth of Biomimetic Microcompartments. *Advanced Biosystems*, 3:1800314, 2019.
- [81] S. Deshpande, S. Wunnavala, D. Hueting, and C. Dekker. Membrane Tension-Mediated Growth of Liposomes. *Small*, 15:1902898, 2019.
- [82] A. Grafmüller, J. C. Shillcock, and R. Lipowsky. The fusion of membranes and vesicles - Pathway and energy barriers from Dissipative Particle Dynamics. *Biophys. J.*, 96:2658–2675, 2009.
- [83] Lianghai Gao, J. Shillcock, and R. Lipowsky. Improved dissipative particle dynamics simulations of lipid bilayers. *J. Chem. Phys.*, 126:015101, 2007.
- [84] P. K.J. Kinnunen. Fusion of lipid bilayers: a model involving mechanistic connection to Hn phase forming lipids. *Chem. Phys. Lipids*, 63:251 – 258, 1992.
- [85] J. M. Holopainen, J. Y. A. Lehtonen, and P.K. J. Kinnunen. Evidence for the Extended Phospholipid Conformation in Membrane Fusion and Hemifusion. *Biophys. J.*, 76:2111 – 2120, 1999.
- [86] H. A. Scheidt, K. Kolocaj, D. B. Konrad, J. A. Frank, D. Trauner, D. Langosch, and D. Huster. Light-induced lipid mixing implies a causal role of lipid splay in membrane fusion. *BBA Biomembranes*, 1862:183438, 2020.
- [87] M. J. Stevens, J. H. Hoh, and T. B. Woolf. Insights into the Molecular Mechanism of Membrane Fusion from Simulation: Evidence for the Association of Splayed Tails. *Phys. Rev. Lett.*, 91(18):188102, 2003.
- [88] K. Pieterse A.F. Smeijers, A.J. Markvoort and A.J. Hilbers. A detailed look at vesicle fusion. *J. Phys. Chem. B*, 110:13212 – 13219, 2006.
- [89] Y.G. Smirnova, S.J. Marrink, R. Lipowsky, and V. Knecht. Solvent-exposed tails as prestalk transition states for membrane fusion at low hydration. *JACS*, 132:6710–6718, 2010.
- [90] D. Mirjanian, A. N. Dickey, J. H. Hoh, T. B. Woolf, and M. J. Stevens. Splaying of Aliphatic Tails Plays a Central Role in Barrier Crossing During Liposome Fusion. *J. Phys. Chem. B*, 114:11061 – 11068, 2010.
- [91] M. A. Tahir, R. C. Van Lehn, S.H. Choi, and A. Alexander-Katz. Solvent-exposed lipid tail protrusions depend on lipid membrane composition and curvature. *Biochim. Biophys. Acta*, 1858:1207 – 1215, 2016.
- [92] J. M. Gardner and C. F. Abrams. Lipid flip-flop vs. lateral diffusion in the relaxation of hemifusion diaphragms. *BBA Biomembranes*, 1860:1452 – 1459, 2018.
- [93] D.P. Siegel. Energetics of intermediates in membrane fusion: Comparison of stalk and inverted micellar intermediate mechanisms. *Biophys. J.*, 65:2124–2140, 1993.

- [94] L. K. Tamm, J. Crane, and V. Kiessling. Membrane fusion: a structural perspective on the interplay of lipids and proteins. *Current Opinion In Struct. Biol.*, 13:453–466, 2003.
- [95] L. V. Chernomordik and M. M. Kozlov. Mechanics of membrane fusion. *Nat. Struct. Mol. Biol.*, 15(7):675 – 683, 2008.
- [96] J. Nikolaus, M. Stoeckl, D. Langosch, R. Volkmer, and A. Herrmann. Direct Visualization of Large and Protein-Free Hemifusion Diaphragms. *Biophys. J.*, 98:1192 – 1199, 2010.
- [97] H. J. Risselada, Y. Smirnova, and H. Grubmüller. Free energy landscape of rim-pore expansion in membrane fusion. *Biophys. J.*, 107:2287–2295, 2014.
- [98] T. Brandt, L. Cavellini, W. Kuehlbrandt, and M. M. Cohen. A mitofusin-dependent docking ring complex triggers mitochondrial fusion in vitro. *eLife*, 5:e14618, 2016.
- [99] M. D’Agostino, H. J. Risselada, L. J. Endter, V. Comte-Miserez, and A. Mayer. SNARE-mediated membrane fusion arrests at pore expansion to regulate the volume of an organelle. *EMBO J.*, 37:e99193, 2018.
- [100] E. M. Blokhuis, M. D’Agostino, A. Mayer, and H. J. Risselada. Fusion Pores Live on the Edge. *J. Phys. Chem. Lett.*, 11:1204 – 1208, 2020.
- [101] H. J. Risselada and H. Grubmüller. How proteins open fusion pores: insights from molecular simulations. *Eur. Biophys. J.*, 50:279 – 293, 2021.
- [102] S. Boonstra, J. S. Blijleven, W. H. Roos, P. R. Onck, E. van der Giessen, and A. M. van Oijen. Hemagglutinin-Mediated Membrane Fusion: A Biophysical Perspective. *Annu. Rev. Biophys.*, 47:153– 173, 2018.
- [103] F. Li. Structure, Function, and Evolution of Coronavirus Spike Proteins. *Annu. Rev. Virol.*, 3:237–261, 2016.
- [104] C. B. Jackson, M. Farzan, B. Chen, and H. Choe. Mechanisms of SARS- CoV-2 entry into cells. *Nat. Rev. Mol. Cell Biol.*, 23:3–20, 2022.
- [105] G. Orso, D. Pendin, S. Liu, J. Tosetto, T. J. Moss, J. E. Faust, M. Micaroni, A. Egorova, A. Martinuzzi, J. A. McNew, and A. Daga. Homotypic fusion of ER membranes requires the dynamin-like GTPase Atlastin. *Nature*, 460:978–983, 2009.
- [106] J. Hu, Y. Shibata, P.-P. Zhu, C. Voss, N. Rismanchi, W. A. Prinz, T. A. Rapoport, and C. Blackstone. A Class of Dynamin-like GTPases Involved in the Generation of the Tubular ER Network. *Cell*, 138:549–561, 2009.
- [107] N. Wang and T. A. Rapoport. Reconstituting the reticular ER network - mechanistic implications and open questions. *J. Cell Sci.*, 132:jcs227611, 2019.
- [108] K. Anwar, R. W. Klemm, A. Condon, K. N. Severin, M. Zhang, R. Ghorlando, J. Hu, T. A. Rapoport, and W. A. Prinz. The dynamin-like GTPase Sey1p mediates homotypic ER fusion in *S. cerevisiae*. *J. Cell Biol.*, 197(2):209–217, 2012.

- [109] M. Zhang and J. Hu. Homotypic fusion of endoplasmic reticulum membranes in plant cells. *Front. Plant Sci.*, 4:Article 514, 2013.
- [110] D. C. Chan. Mitochondrial Fusion and Fission in Mammals. *Annu. Rev. Cell Dev. Biol.*, 22:79 – 99, 2006.
- [111] L. Tilokani, S. Nagashima, V. Paupe, and J. Prudent. Mitochondrial dynamics: overview of molecular mechanisms. *Essays Biochem*, 62:341 – 360, 2018.
- [112] A. Green, T. Hossain, and D. M. Eckmann. Mitochondrial dynamics involves molecular and mechanical events in motility, fusion and fission. *Front. Cell Dev. Biol.*, 10:1010232, 2022.
- [113] R. Jahn and R. H. Scheller. SNAREs — engines for membrane fusion. *Nat. Rev. Mol. Cell Biol.*, 7:631 – 643, 2006.
- [114] S. Koike and R. Jahn. SNARE proteins: zip codes in vesicle targeting? *Biochem. J.*, 479:273 – 288, 2022.
- [115] D. Mion, L. Bunel, P. Heo, and F. Pincet. The beginning and the end of SNARE-induced membrane fusion. *FEBS Open Bio*, 12:1958 – 1979, 2022.
- [116] A. Nowbagh, A. Deshwal, M. Kadu, A. Chaudhuri, S. Maiti, R. Lipowsky, and T. Bhatia. Generation of Bilayer Asymmetry and Membrane Curvature by the Sugar-Cleaving Enzyme Invertase. *ChemSystemsChem*, 5:e202200027, 2022.
- [117] C. Delaunay. Sur la surface de révolution dont la courbure moyenne est constante. *J. Math. Pures et Appl. Sér. 1*, 6:309–320, 1841.
- [118] N. Kapouleas. Complete Constant Mean Curvature Surfaces in Euclidean Three-Space. *Ann. Math.*, 131:239–330, 1990.
- [119] N. J. Korevaar, R. Kusner, and B. Solomon. The Structure of Complete Embedded Surfaces with Constant Mean Curvature. *J. Differential Geometry*, 30:465–503, 1989.
- [120] N. Korevaar and R. Kusner. The global structure of constant mean curvature surfaces. *Invent. math.*, 114:311–332, 1993.
- [121] K. Grosse-Brauckmann and K. Polthier. Constant Mean Curvature Surfaces Derived from Delaunay’s and Wente’s Examples. In H. C. Hege and K. Polthier, editors, *Visualization and Mathematics*, page 386. Springer Verlag, 1997.
- [122] K. Grosse-Brauckmann, R. B. Kusner, and J. M. Sullivan. Triunduloids: embedded constant mean curvature surfaces with three ends and genus zero. *Journal für die reine und angewandte Mathematik*, 564:35–61, 2003.
- [123] R. Lipowsky, S. Pramanik, A. S. Benk, J. Spatz, and R. Dimova. Elucidating the Morphology of the Endoplasmic Reticulum: Puzzles and Perspectives. *ACS Nano*, 17:11957–11968, 2023.
- [124] R. E. Powers, S. Wang, T. Y. Liu, and T. A. Rapoport. Reconstruction of the tubular endoplasmic reticulum network with purified components. *Nature*, 543:257–272, 2017.

- [125] M. A. Betancourt-Solis, T. Desai, and J. A. McNew. The atlastin membrane anchor forms an intramembrane hairpin that does not span the phospholipid bilayer. *J. Biol. Chem.*, 293(48):18514–18524, 2018.
- [126] D. Holcman, P. Parutto, J. E. Chambers, M. Fantham, L. J. Young, S. J. Marciniak, C. F. Kaminski, D. Ron, and E. Avezov. Single particle trajectories reveal active endoplasmic reticulum luminal flow. *Nat. Cell Biol.*, 20:1118–1125, 2018.
- [127] R. Sender and R. Milo. The distribution of cellular turnover in the human body. *Nature Medicine*, 27:45–48, 2021.
- [128] C. Kötting and K. Gerwert. What vibrations tell us about GTPases. *Biol. Chem.*, 396:131–144, 2015.